



Multi-scale fission product release model with comparison to AGR data

June 30, 2023

Technical Report

Pierre-Clément A. Simon¹, Larry K. Aagesen¹, Chaitanya Bhawe¹,
Chao Jiang¹, Wen Jiang¹, Jia-Hong Ke¹, and Lin Yang¹

¹Idaho National Laboratory



DISCLAIMER

This information was prepared as an account of work sponsored by an agency of the U.S. Government. Neither the U.S. Government nor any agency thereof, nor any of their employees, makes any warranty, expressed or implied, or assumes any legal liability or responsibility for the accuracy, completeness, or usefulness, of any information, apparatus, product, or process disclosed, or represents that its use would not infringe privately owned rights. References herein to any specific commercial product, process, or service by trade name, trade mark, manufacturer, or otherwise, does not necessarily constitute or imply its endorsement, recommendation, or favoring by the U.S. Government or any agency thereof. The views and opinions of authors expressed herein do not necessarily state or reflect those of the U.S. Government or any agency thereof.

Multi-scale fission product release model with comparison to AGR data

Technical Report

Pierre-Clément A. Simon¹, Larry K. Agesen¹, Chaitanya Bhawe¹, Chao Jiang¹, Wen Jiang¹,
Jia-Hong Ke¹, and Lin Yang¹

¹Idaho National Laboratory

June 30, 2023

**Idaho National Laboratory
Computational Mechanics and Materials Department
Idaho Falls, Idaho 83415**

<http://www.inl.gov>

**Prepared for the
U.S. Department of Energy
Office of Nuclear Energy
Under U.S. Department of Energy-Idaho Operations Office
Contract DE-AC07-05ID14517**

Page intentionally left blank

Abstract

TRistructural ISOtropic (TRISO) particle fuel is central to several advanced, high-temperature reactor designs. Each particle consists of a fuel kernel encapsulated by three layers of carbon and ceramics that prevent the release of fission products and ensure physical integrity. Despite outstanding retention properties, fission product release has been observed from intact particles. To better understand and quantify fission product release from TRISO particles, a multiscale, mechanistic model of fission product transport is being developed by the Nuclear Energy Advanced Modeling and Simulation (NEAMS) program. Previous work focused on silver (Ag) transport and improved Ag release predictions. The work described in this report builds on this experience to better understand cesium (Cs) transport in silicon carbide (SiC), the main barrier to the release of fission products. Atomistic simulations provide bulk and grain boundary (GB) Cs diffusivities in SiC, which are used by phase field simulations in the mesoscale code Marmot to determine the temperature, microstructure, and irradiation-dependent Cs diffusivity at the mesoscale in SiC. This approach attributes the different temperature regimes experimentally observed for Cs diffusivities in SiC to a transition from bulk-dominated diffusivity at high temperatures to a GB-dominated regime at low temperatures, providing new insight. The multiscale, mechanistic effective diffusivity is then implemented in the fuel performance code BISON and further validated by comparing Cs release predictions from Advanced Gas Reactor (AGR)-1 and AGR-2 post-irradiation measurements. The new model improves BISON's predictability. This document also reports improvements made on Ag transport modeling by accounting for different GB types having different diffusivities. Moreover, this report details preliminary efforts to model palladium (Pd) attack of the SiC at the mesoscale using a phase field approach. Pd attack and its impact on accelerated Ag transport remains a misunderstood phenomenon, and we use the model to demonstrate that the formation of lamellae that has been observed in experiments can be explained by the reaction of Pd with SiC to form alternating layers of graphite and Pd_2Si . This effort aims to improve our understanding of the reaction and eventually provide a model for BISON to account for Pd penetration and its effects on fission product release.

Page intentionally left blank

Acknowledgments

This report was authored by a contractor of the U.S. Government under contract DE-AC07-05ID14517. Accordingly, the U.S. Government retains a non-exclusive, royalty-free license to publish or reproduce the published form of this report, or allow others to do so, for U.S. Government purposes. Funding was provided by the Nuclear Energy Advanced Modeling and Simulation (NEAMS) program.

This research made use of the resources of the High Performance Computing Center at Idaho National Laboratory, which is supported by the DOE Office of Nuclear Energy and the Nuclear Science User Facilities under contract no. DE-AC07-05ID14517.

Page intentionally left blank

Contents

Abstract	iv
List of Figures	ix
List of Tables	xiii
Acronyms	xiv
1 INTRODUCTION	1
2 DETERMINATION OF BULK Cs DIFFUSIVITY IN SiC	5
2.1 Atomistic calculation of Cs diffusivity in SiC enhanced by irradiation	5
2.2 Fitting the irradiation-enhanced Cs diffusivity in bulk SiC to be used at the mesoscale	10
3 DETERMINATION OF GB Cs DIFFUSIVITY IN SiC	12
4 DEVELOPMENT AND VALIDATION OF A MESO-SCALE EFFECTIVE Cs DIFFUSIVITY IN SiC	18
4.1 Description of the SiC microstructures	18
4.2 Method for effective diffusivity calculations	19
4.3 Effective diffusivity calculations	20
4.4 Improvement of the Cs effective diffusivity calculations	24
5 VALIDATION OF THE EFFECTIVE Cs DIFFUSIVITY IN SiC USING AGR-1 AND AGR-2 DATA	29
6 PALLADIUM ATTACK OF SiC	31
6.1 Description of the Pd attack of SiC	31
6.2 Model development	31
6.3 Discussion	38
7 IMPROVEMENT OF THE MODEL FOR Ag DIFFUSION IN SiC	40
7.1 New estimate of Ag diffusion in SiC in different GB types using a new potential for molecular dynamics (MD) calculations	40
7.2 Impact on mesoscale effective Ag diffusivity in SiC	40
8 OVERALL CONCLUSIONS AND FUTURE WORK	53
Bibliography	55

List of Figures

1.1	Graph of Cs diffusivities in SiC reported in the literature based on experimental (ion implantation and integral release fitting) and modeling (density functional theory (DFT) and MD) approaches [14, 15, 16, 17, 18, 19, 20, 21, 24, 9, 8, 22, 23, 12, 13]. The values are listed in Table 1.1. Experimental observations show two temperature regimes with a transition around 1800 K, which is not reproduced by modeling efforts. Note that th. and irr. stand for thermal and irradiation, respectively.	3
2.1	Plots showing the diffusion coefficient of Cs in bulk SiC as a function of reciprocal temperature. The solid blue and red lines show the calculated radiation-enhanced diffusion coefficient of Cs in bulk SiC under the AGR-1 conditions. The dashed lines are the thermal diffusion coefficient of Cs under thermodynamic equilibrium of the vacancy concentration.	9
2.2	Binding energies of different vacancy clusters in SiC calculated by DFT. The green color indicates the mixed clusters, and the blue color indicates the carbon vacancy clusters.	10
2.3	Fitting the irradiation-enhanced bulk Cs diffusion as a function of flux. (a) shows how D_0^{irr} evolves with the flux and how it was fitted using Eq. (2.10), and (b) shows how Q^{irr} evolves with the flux and how it was fitted using Eq. (2.11). (c) shows the final fit for $D_{bulk}(T, F)$ described in Eq. (2.7).	11
3.1	Comparison between DFT-calculated and ABOP-calculated formation energies of Cs and Ag in SiC. The solid lines represent perfect agreement between DFT and new empirical potentials developed in this work.	13
3.2	$\Sigma 5$ (210)/[001] GB of SiC. The green and red spheres represent Si and C atoms, respectively.	14
3.3	MSD data for Cs and Ag atoms diffusing within the $\Sigma 5$ (210)/[001] GB of SiC at various temperatures.	15
3.4	Arrhenius plot for Cs and Ag diffusivities within the $\Sigma 5$ (210)/[001] GB of SiC. The solid lines represents the best fitting of MD data using the Arrhenius equation.	16
3.5	Arrhenius plot for Cs and Ag diffusivities within the random HAGBs of SiC. Results for $\Sigma 5$ (210)/[001] GB are also shown for comparison. The solid lines represents the best fitting of MD data using the Arrhenius equation.	17
4.1	Comparison of the bulk and GB diffusivities with the empirical fit from Christ [21] used in BISON, and the data points obtained from the mesoscale simulations. The red dots show the effective diffusivities obtained when assuming that all GBs are diffusing as $\Sigma 5$ GBs; the purple dots show the effective diffusivities obtained when assuming that all GBs are diffusing as high-angle grain boundary (HAGB)s.	20
4.2	Derivation of the thermal contribution to the effective Cs diffusion coefficient as a function of the temperature T , the grain minor axis length m_j , and the grain major axis length m_a	22
4.3	Influence of (a) temperature, (b) irradiation flux, and (c,d) grain major and minor axis lengths on the irradiation-enhanced diffusion contribution	24

4.4	Comparison of the Cs diffusion coefficients provided by atomistic simulations (i.e., the temperature and irradiation-dependent bulk D_{bulk} derived in Chapter 2 and the GB D_{GB} Chapter 3), the empirical coefficient D_{Christ} used in BISON [21], and the mesoscale effective diffusivity models from the current study $D^{eff,tot}$ (Eqs. (4.4) to (4.7)). $D_{\Sigma 5}^{eff,tot}$ and $D_{HAGB}^{eff,tot}$ assume that all the GBs are $\Sigma 5$ or HAGB GBs, respectively. The range between the full and dotted lines for $D^{eff,tot}$ correspond to extreme grain minor axis length values of the SiC microstructures described in Section 4.1.	25
4.5	Derivation of the thermal contribution to the effective Cs diffusion coefficient as a function of the temperature T , the grain minor axis length m_i , and the grain major axis length m_a with a reduced HAGB diffusivity.	26
4.6	Influence of (a) temperature, (b) flux, and (c,d) grain major and minor axis lengths on the irradiation-enhanced diffusion contribution (C^{irr} from Eq. (4.7)) in polycrystalline SiC microstructures, with a reduced HAGB diffusivity. This figure is the equivalent of Fig. 4.3 but with a HAGB diffusivity divided by 100. The trends and conclusion remain similar.	27
4.7	Comparison of the atomistic and modified effective diffusivities with the empirical model from Ref. [21]. The modified effective diffusivity model is similar to the model presented in Fig. 4.7, but with a HAGB diffusivity divided by 100. The modified diffusivity better matches the empirical model.	28
5.1	Comparison of measured (post-irradiation examination) and computed (BISON) Cs release fractions for AGR-1 and AGR-2 compacts.	30
6.1	Free energy of Pd-Si-C system as a function of the composition at $T = 1200$ K. Graphite is the only substitutional phase and has a non-convex free energy function. All other phases are stoichiometric compounds.	33
6.2	Effect of D_C/D_{Pd} on microstructure formed during Pd attack of SiC. The graphite, Pd_2Si and SiC phases are represented by grey, red, and orange colors, respectively. (a) shows the initial condition of the system. (b), (c), (d), (e), and (f) show the microstructure formed after 10^6 s with the ratio of D_C/D_{Pd} set to 10^0 , 10^{-1} , 10^{-2} , 10^{-3} , and 10^{-4} , respectively. As the carbon diffusivity becomes smaller, the graphite and Pd_2Si start growing in bands perpendicular to the direction of Pd flux.	36
6.3	Effect of Pd flux J_{Pd} on microstructure formed during Pd attack of SiC. The graphite, Pd_2Si , and SiC phases are represented by grey, red, and orange colors, respectively. (a) shows the initial condition of the system. (b) and (c) show the microstructure formed after 10^5 s with $J_{Pd} = 2.074 \times 10^{-6}$ atoms $s^{-1}nm^{-2}$ and 10^6 s with $J_{Pd} = 2.074 \times 10^{-7}$ $s^{-1}nm^{-2}$, respectively. In both cases, the total amount of Pd entering the system is same, and the total increase in Pd_2Si and graphite phases is the the same. The lower Pd flux results in growth of the pre-existing phases, whereas the higher flux in (b) causes the nucleation and growth of new Pd_2Si and graphite regions.	36
6.4	Simulating Ni-Cr corrosion in molten FLiBe salt. The solid lines show the atomic fraction of the Ni and Cr, and the dotted lines show the chemical potential calculated by solving the equipotential condition. (a) shows the initial condition of the system; (b) shows the chemical potential evolution after 10^4 s. . .	38
7.1	Arrhenius plot for Cs and Ag diffusivities within the $\Sigma 5$ (210)/[001] GB of SiC. The solid lines represent the best fitting of MD data using the Arrhenius equation.	41

7.2	Comparison of the Ag diffusion coefficients provided by atomistic simulations (bulk diffusivity, HAGB diffusivity, and LAGB diffusivity), the empirical coefficient D_{emp}^{BISON} previously used in BISON [14, 62, 1, 63], and the effective Ag diffusivity values provided by the current mesoscale study $D^{eff,tot}$ for Ag—Eqs. (4.4) to (4.6). The different values for $D^{eff,tot}$ at each temperature correspond to the extreme grain minor axis length values of the SiC microstructures described in Section 4.1 (solid line for smallest minor axis size, dashed lines for largest minor axis size) and different flux values ($D^{eff,tot}$ for 0 flux, $D^{eff,tot}(F)$ for flux = 4.7×10^{17} n/m ² /s).	42
7.3	Comparison of the Ag diffusion coefficients provided by old atomistic simulations with GB diffusivity of higher activation energy (bulk diffusivity, HAGB diffusivity, and LAGB diffusivity) [3], the empirical coefficient D_{emp}^{BISON} previously used in BISON [14, 62, 1, 63], and the effective Ag diffusivity values provided by the current mesoscale study $D^{eff,tot}$ for Ag—Eqs. (4.4) to (4.6). The different values for $D^{eff,tot}$ at each temperature correspond to the extreme grain minor axis length values of the SiC microstructures described in Section 4.1 (solid line for smallest minor axis size, dashed lines for largest minor axis size), and different flux values ($D^{eff,tot}$ for 0 flux, $D^{eff,tot}(F)$ for flux = 4.7×10^{17} n/m ² /s).	43
7.4	Examples of microstructures with mixed GB types with different LAGB fractions. The yellow GBs are HAGBs, and the green GBs are LAGBs. The LAGB fractions are (a) 0.3, (b) 0.5, (c) 0.7, and (d) 0.9.	44
7.5	One smoothed microstructure after grain growth. (a) is the smoothed microstructure; (b) is the microstructure with distinguished GB type. In (b), grain interiors are shown in blue, LAGBs are shown in grey, and HAGBs are shown in red.	45
7.6	One microstructure distinguished by Grain Tracker feature in MOOSE. (a) shows the unique index of LAGBs; (b) shows the unique index of LAGB clusters.	47
7.7	Comparison of the Ag diffusion coefficients provided by atomistic simulations with GB diffusivity of higher activation energy (bulk diffusivity, HAGB diffusivity, and LAGB diffusivity) [3], the empirical coefficient D_{emp}^{BISON} previously used in BISON [14, 62, 1, 63], and the effective Ag diffusivity values provided by the current mesoscale study $D^{eff,tot}$ for Ag, including percolation effects (dots). The different values for $D^{eff,tot}$ at each temperature correspond to the extreme grain minor axis length values of the SiC microstructures described in Section 4.1 (solid line for smallest minor axis size, dashed lines for largest minor axis size), and different flux values ($D^{eff,tot}$ for 0 flux, $D^{eff,tot}(F)$ for flux = 4.7×10^{17} n/m ² /s).	48
7.8	Example of a microstructure with different GB type distributions. (a) is the base microstructure; (b, c) show the unique LAGB cluster index with different GB type distributions: (b) has no channel, and (c) has one LAGB channel.	50
7.9	Derivation of the percolation contribution to the effective Ag diffusion coefficient as a function of temperature T and different percolation definitions P . (a,b,c) show how (a) D_0^{perco} and (b) C^{perco} depend on T , and (c) shows how $D^{eff,tot,perco}$ depends on P at 1000 K when $P = f_{num}$. (d,e,f) show how (d) D_0^{perco} and (e) C^{perco} depend on T , and (f) shows how $D^{eff,tot,perco}$ depends on P at 1000 K when $P = f_{area}$. (g,h,i) show how (g) D_0^{perco} and (h) C^{perco} depend on T , and (i) shows how $D^{eff,tot,perco}$ depends on P at 1000 K when $P = s_{cluster}$. (j,k,l) show how (j) D_0^{perco} and (k) C^{perco} depend on T , and (l) shows how $D^{eff,tot,perco}$ depends on P at 1000 K when $P = L_{cluster}$. In (c,f,i,l), the effective diffusivity of microstructures with an LAGB channel is noted by a star label; others are noted by a point label.	51

7.10	Derivation of the flux contribution to the effective Ag diffusion coefficient as a function of temperature T , minor axis m_i , flux F , and different percolation definitions P . (a,b,c,d) show how $C^{irr,perco}$ depends on (a) T , (b) m_i , (c) F , and (d) P when $P = f_{num}$. (e,f,g,h) show how $C^{irr,perco}$ depends on (e) T , (f) m_i , (g) F , and (h) P when $P = f_{area}$. (i,j,k,l) show how $C^{irr,perco}$ depends on (i) T , (j) m_i , (k) F , and (l) P when $P = s_{cluster}$. (m,n,o,p) show how $C^{irr,perco}$ depends on (m) T , (n) m_i , (o) F , and (p) P when $P = L_{cluster}$.	52
------	---	----

List of Tables

1.1	Summary of Cs diffusivities in SiC reported in the literature, partly inspired from [8] with updates and corrections. The th. and irr. stand for thermal and irradiation, respectively.	2
2.1	DFT calculation results of all migration barriers of hops described in Section 2.1.	7
4.1	Parameter values for the mesoscale effective diffusion described in Eqs. (4.4) to (4.7).	23
4.2	Parameter values for the mesoscale effective diffusion described in Eqs. (4.4) to (4.7) but with the HAGB diffusivity reduced by a factor of 100.	25
5.1	Microstructure properties of AGR-1 and AGR-2 fuel capsules obtained from cross-referencing Ref. [33] and Table 6 from Ref. [40]. Optimized values are determined by comparing model's predictions against PIE data.	29
6.1	Material property values for the Pd-Si-C system	34

Accronyms

TRISO	TRistructural ISOtropic
SiC	silicon carbide
Ag	silver
Cs	cesium
Pd	palladium
GB	grain boundary
AGR	Advanced Gas Reactor
MD	molecular dynamics
DFT	density functional theory
NEAMS	Nuclear Energy Advanced Modeling and Simulation
HAGB	high-angle grain boundary
LAGB	low-angle grain boundary

1. INTRODUCTION

Tristructural isotropic (TRISO) particle fuel is central to several advanced, high-temperature reactor designs. A TRISO particle contains a fuel kernel at its center, which is coated with a porous carbon buffer layer, an inner pyrolytic carbon (IPyC) layer, a silicon carbide (SiC) layer, and an outer pyrolytic carbon (OPyC) layer [1]. The different layers ensure the physical integrity of the particle and prevent the release of fuel and fission products. In particular, the SiC is the main barrier for the release of silver (Ag) and cesium (Cs). Despite outstanding retention properties, fission product release has been observed out of intact particles [2].

To understand and quantify fission product release from TRISO fuel particles, experimental and modeling efforts have evaluated the diffusivity of fission products in the different layers. The diffusivities of Ag and Cs in SiC have been of particular interest since they are the most prevalent released species, and the SiC layer acts as the main barrier to release. To support that effort, the Department of Energy's Nuclear Energy Advanced Modeling and Simulation (NEAMS) program aims to develop multi-scale, mechanistic models of Ag and Cs diffusivity in SiC to accurately predict their potential release from TRISO particles. Previous work has been successful in developing a validated, effective diffusivity for Ag in SiC that accounts for temperature, grain size, and irradiation levels [3, 4, 5]. This approach leveraged density functional theory (DFT) and molecular dynamics (MD) to determine bulk and grain boundary (GB) Ag diffusivity and combined them in a phase field model using the mesoscale fuel performance code Marmot [6] to derive an effective diffusivity that could be used in the engineering scale fuel performance code BISON [7]. Using this mechanistic approach provided important insights: (1) GB diffusivity was determined to be several orders of magnitude higher than the bulk diffusivity, as expected [3]; (2) the SiC grain size in the direction perpendicular to Ag transport was found to have the strongest impact on the effective diffusion coefficient because small grain size in that direction leads to a higher number of GBs in the direction of Ag transport, which act as high-diffusivity pathways [3, 4]; (3) irradiation effects were found to be minimal at the levels used in the Advanced Gas Reactor (AGR) program and affected Ag release only at low temperatures [5]. Moreover, it was found that the BISON predictions were consistently improved by using this mechanistic approach over the commonly used empirical fit for Ag diffusivity in SiC [3, 4, 5].

The work detailed in this report uses the proven approach deployed in previous work to develop a multi-scale, mechanistic, effective diffusivity model for Cs in SiC. We will use (1) DFT, kinetic Monte Carlo, and rate theory to derive the bulk Cs diffusivity in SiC as a function of temperature and neutron flux, (2) MD to determine Cs diffusivity in HAGB and $\Sigma 5$ GB, and (3) combine these results in a mesoscale phase field approach to derive an effective diffusivity that can be used in a fuel performance code (e.g., BISON). Previous experimental (ion implantation and integral release fitting) and modeling efforts (DFT and MD) have quantified Cs diffusivity in SiC, and a summary of the results can be

found in Table 1.1 and Fig. 1.1.

As shown in Fig. 1.1, experimental observations show two temperature regimes with a transition around 1800 K, which is not reproduced by modeling efforts. The mechanisms behind these two temperature regimes is currently unknown, although several hypotheses exist. One hypothesis, proposed by Malherbe et al. in [2], states that the enhanced diffusivity at high temperatures can be attributed to the de-trapping of Cs atoms from irradiation-induced defects in bulk SiC at high temperatures, which are then able to diffuse. Another hypothesis explains these trends with a balance between bulk and GB diffusivities, as described by several authors, including in [8, 9]. GB diffusivity is thought to dominate at low temperatures due to a lower activation energy, while bulk diffusivity, representing the majority of the volume fraction, would dominate at high temperatures where bulk and GB diffusivities are closer to each other. The multi-scale, mechanistic approach described above enables the testing of these two hypotheses and the quantitative investigation, for the first time with modeling tools, of the mechanisms behind the two temperature regimes observed in Cs diffusivity in SiC.

Table 1.1. Summary of Cs diffusivities in SiC reported in the literature, partly inspired from [8] with updates and corrections. The th. and irr. stand for thermal and irradiation, respectively.

Reference	Temperature range (K)	$D_{0,1}$ (m^2s^{-1})	Q_1 (kJ/mol)	$D_{0,2}$ (m^2s^{-1})	Q_2 (kJ/mol)
Ion implantation					
Friedland [10, 11]	1273.15 - 1773.15	-	-	-	-
Dwaraknath th. bulk [12]	1173.15 - 1573.15	2.1×10^{-17}	96	-	-
Dwaraknath th. GB [12]	1173.15 - 1573.15	-	-	-	-
Dwaraknath irr. bulk [13]	1173.15 - 1373.15	1.7×10^{-21}	-39	-	-
Dwaraknath irr. GB [13]	1173.15 - 1373.15	-	-	-	-
Integral release fitting					
Moormann [14]	973.15 - 1773.15	1.8×10^{-11}	176	-	-
Myers - upper [15]	Unknown	6.68×10^{-14}	106	2.37×10^{-2}	482
Myers - lower [15]	Unknown	6.68×10^{-14}	106	1.12×10^{-4}	437
Minato [16]	1873.15 - 2173.15	2.5×10^{-2}	503	-	-
Amian [17]	1273.15 - 1873.15	3.5×10^{-9}	236.6	-	-
Gudkov [18]	1273.15	2.3×10^{-17}	-	-	-
Fukuda [19]	1473.15 - 1673.15	6.8×10^{-12}	177	-	-
Ogawa - upper [20]	1573.15 - 1773.15	2.8×10^{-4}	420	-	-
Ogawa - lower [20]	1573.15 - 1773.15	1.5×10^{-4}	422	-	-
Christ [21]	Unknown	$5.5 \times 10^{-14} \exp\left(\frac{F}{F_{ref}}\right)$	125	1.6×10^{-2}	514
Verfondern [22]	1873.15 - 2073.15	1.58×10^{-2}	514	-	-
Allelein [23]	1273.15 - 1773.15	1.50×10^{-11}	175	-	-
Modeling					
Rabone $\Sigma 5$ GB - upper [24]	1500	1.21×10^{-6}	424	-	-
Rabone $\Sigma 5$ GB - lower [24]	1500	1.21×10^{-6}	474	-	-
Shrader Bulk 3C-SiC [9]	Unknown	5.10×10^{-8}	496	-	-
Ko HEGB - upper [8]	1473.15 - 1873.15	$(3.75+3.15) \times 10^{-11}$	207	-	-
Ko HEGB - lower [8]	1473.15 - 1873.15	$(3.75-3.15) \times 10^{-11}$	258	-	-

In addition to the focus on Cs diffusivity in SiC, we report recent improvements made to the effective Ag diffusivity

model by introducing different diffusivities for HAGBs and $\Sigma 5$ GBs and linking SiC texture to effective Ag diffusivity. Moreover, we attempted to better understand palladium (Pd) attack of SiC and its effect on the potentially accelerated release of fission products from TRISO particles. The preliminary NEAMS efforts focusing on atomistic simulations of Pd attack [5] were complemented with a new mesoscale approach to identify potential key mechanisms.

In this report, we detail advancements made (1) in developing a multi-scale, mechanistic Cs diffusivity in SiC and validating it using AGR data, (2) in investigating key mechanisms of Pd attack in SiC at the mesoscale, and (3) in improving the model for Ag diffusivity in SiC to account for previously neglected mechanisms. In Chapters 2 and 3, we use atomistic simulations to determine the bulk and GB diffusivities of Cs in SiC, respectively. In Chapter 4,

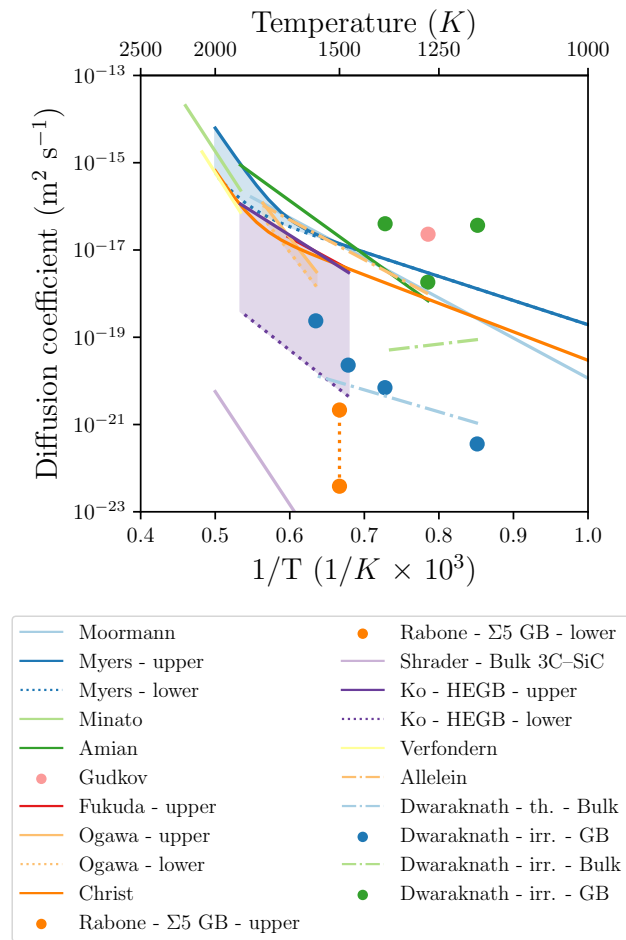


Figure 1.1. Graph of Cs diffusivities in SiC reported in the literature based on experimental (ion implantation and integral release fitting) and modeling (DFT and MD) approaches [14, 15, 16, 17, 18, 19, 20, 21, 24, 9, 8, 22, 23, 12, 13]. The values are listed in Table 1.1. Experimental observations show two temperature regimes with a transition around 1800 K, which is not reproduced by modeling efforts. Note that th. and irr. stand for thermal and irradiation, respectively.

we leverage these results to develop an effective Cs diffusivity in SiC, which is compared against experimental data and other modeling efforts. In Chapter 5, we validate the predictions of the new effective Cs diffusivity against fission product release data from the AGR program. The mesoscale effort to understand Pd attack is then reported in Chapter 6, and new development for Ag diffusivity in SiC are detailed in Chapter 7. Finally, in Chapter 8, conclusions are drawn, and an outlook for further work is given.

2. DETERMINATION OF BULK Cs DIFFUSIVITY IN SiC

2.1 Atomistic calculation of Cs diffusivity in SiC enhanced by irradiation

Following the previous milestones for Ag transport in SiC [3, 5, 4], the diffusion coefficients of Cs in SiC under thermal and irradiated conditions are calculated. The calculations are under the assumption that carbon vacancies are the main mobile carriers for the diffusion of fission products, including Cs and Ag. The assumption is supported by the fact that compared to the silicon vacancy, the carbon vacancy in SiC has a lower formation energy. Additionally, simulation studies of defect production in irradiated SiC performed by molecular dynamics have shown that carbon vacancies outnumber silicon vacancies in displacement cascades over a wide range of primary knock-on atom energies [25]. DFT calculations were first performed to derive the migration barriers of Cs and carbon close to the vicinity of the Cs atom, following the symmetrically unique diffusion paths as determined in [3]. Atomistic kinetic Monte Carlo (kMC) simulations are performed by assuming the effect of Cs on the vacancy-mediated hopping diminishes as the vacancy is beyond the 2nd nearest neighbor from the Cs atom. The vacancy mobility and Cs diffusion coefficient determined by kMC are then used to inform the rate theory model to calculate the excess carbon vacancy concentration as well as the enhanced diffusion coefficients of Cs.

A total of 12 symmetrically nonequivalent vacancy-atom hops are considered in the study of Cs substitutional diffusion in SiC. The work reasons that the diffusion paths causing the formation of anti-site defects are energetically unfavorable, and thus their contributions to Cs diffusion can be considered negligible. In this work, the hops associated with the $\text{Cs}_\text{C}-\text{Va}_\text{C}$ and $\text{Cs}_\text{Si}-\text{Va}_\text{C}$ Cs-vacancy pairs were considered. The associated atomic hops considered in this study are summarized briefly. Please refer to the graphics in [3] for more details. For the hopping paths associated with the $\text{Cs}_\text{C}-\text{Va}_\text{C}$ pair, the multifrequency hops of C are similar to those of the five-frequency model for the face-centered cubic (fcc) system. The hops of vacancy-Cs exchange, vacancy rotation, and dissociation/association include seven symmetrically nonequivalent hopping paths on the (111) lattice plane of SiC. The rotation hops associated with the $\text{Cs}_\text{C}-\text{Va}_\text{C}$ pair consist of two unique paths. For the first (second) types of rotation hops, the nearest Si atom shared with the moving C atom and vacancy is the first (second) nearest neighbor Si atom with respect to C. Since the hopping path of the type-I rotation hops may cause more displacement of the silicon atom that is located at the center of the $3\text{C}-1\text{Cs}$ tetrahedron, the migration barrier of the type-I rotation hop is expected to be higher than that of the type-II rotation hop. The vacancy-Cs dissociation/association hops from/to the second, third, and fourth nearest-neighbor

positions with respect to the Cs atom are determined. For each of the second and fourth dissociation/association hops, there is only one symmetrically nonequivalent hop in each case. There are two different third dissociation/association hops. For the first (second) type of third dissociation/association hops, the nearest Si atom shared with the moving C atom and vacancy is the second (third) nearest neighbor Si atom with respect to C. The vacancy-atom hops associated with the $\text{Cs}_{\text{Si}}\text{-Va}_{\text{C}}$ pair consist of four symmetrically nonequivalent paths, including vacancy-Cs exchange, vacancy rotation, and second and third nearest-neighbor dissociation/association. Note that there is only a single type of rotation hop associated with the $\text{Cs}_{\text{Si}}\text{-Va}_{\text{C}}$ pair.

The ground state energies and migration barriers are calculated using the Vienna Ab initio Simulation Package (VASP). All calculations were spin-polarized and initialized under the ferromagnetic ordering. The plane wave energy cutoff was selected to be 600 eV for all calculations. The interactions between ions and core electrons are described using the projector augmented wave (PAW) method. The Perdew-Burke-Ernzerhof parameterization of the generalized gradient approximation was used for the exchange correlation potentials. The Brillouin zone was sampled using a $4 \times 4 \times 4$ k-point mesh generated using the Monkhorst-Pack scheme. Calculations were performed with a 216-site periodic simulation cell, which is a $3 \times 3 \times 3$ supercell of the zinc blende (sphalerite) unit cells of SiC. The transition state and migration barrier were determined by climbing-image nudged-elastic-band (CI-NEB) calculations [26]. The Quick-Min force-based optimizer was used to determine the minimum energy paths and saddle points, and the optimizer was implemented by the Transition State Tools for VASP (VTST). In all ground-state DFT and CI-NEB runs, the break condition of energy convergence for electronic relaxation is 10^{-6} eV, and force for ionic relaxation is 0.01 eV/Å.

Table 2.1 shows the migration barriers of all symmetrically unique hops calculated by using DFT and CI-NEB methods, including both the results of Ag and Cs. It can be seen that the diffusion of Cs is very similar to Ag in terms of the migration barrier and binding energy (difference in associating and dissociating migration barrier). Both Cs and Ag have a lower energy barrier for the exchange hop compared to the rotation hops. The two fission product atoms at the carbon site have a strong binding with the carbon vacancy, while the binding is even more pronounced for the mixed $\text{X}_{\text{Si}}\text{-Va}_{\text{C}}$ pair ($\text{X}=\text{Ag}$ and Cs). Note that in Table 2.1, the data marked by * indicate that the initial and end ground state configurations relaxed to the same structure during structural relaxation during DFT calculations. The data marked by N/A for one of the $\text{Va}_{\text{C}}\text{-Cs}_{\text{C}}$ associating/dissociating hops is not available because of an electronic convergence issue during structural optimization, possibly caused by the ferromagnetism of the Cs atom.

The kMC simulations were performed using the migration barriers derived by DFT. The kinetic model assumes the atomic hops beyond the range of the hops listed in Table 2.1 will be the same as the diffusion events in SiC without Cs. The kMC model implemented the kinetically resolved activation (KRA) barriers to determine the hopping events. The KRA barriers were calculated from the ground-state and transition-state energies. The attempt frequencies of all vacancy-mediated hops are assumed to be 5×10^{12} Hz. The $20 \times 20 \times 20$ supercell of the primitive unit cell was used with a total of 16,000 atomic sites, including 1 Cs atom and 1 carbon vacancy in a SiC background supercell. Each kMC run was initiated with 100 passes for configuration equilibration, followed by 10,000 passes to determine the diffusion coefficient, which was sampled in a period of 10 passes. KMC runs were performed for temperatures from 1073 to 2073 K. The tracer diffusion coefficient of Cs can then be determined as

$$D_{\text{Cs}}^* = 4.7 \times 10^{-4} \exp \left(-\frac{5.54 \pm 0.68 \text{ (eV)}}{k_B T} \right) (\text{m}^2/\text{s}). \quad (2.1)$$

Note that the range of the activation energy in Eq. 2.1 is caused by the uncertainty of vacancy formation energy and the binding energy of the Cs_C - Va_C pair.

Table 2.1. DFT calculation results of all migration barriers of hops described in Section 2.1.

Description of hops	Moving species	X=Ag, barrier (eV)	X=Cs, barrier (eV)
No X			
Va_{Si} exchange with Si_{Si}	Si	3.59	3.59
Va_C exchange with C_C	C	3.51	3.51
X_C-Va_C pair			
Va_C exchange with X_C	X	2.27	2.45
Va_C rotate X_C (I)	C	4.38	5.05
Va_C rotate X_C (II)	C	3.26	0.01*
Va_C dissociate from X_C , 2nn	C	4.90	5.25
Va_C associate to X_C , 2nn	C	2.06	2.47
Va_C dissociate from X_C , 3nn (I)	C	4.51	4.88
Va_C associate to X_C , 3nn (I)	C	1.87	2.17
Va_C dissociate from X_C , 3nn (II)	C	4.40	N/A
Va_C associate to X_C , 3nn (II)	C	2.20	N/A
Va_C dissociate from X_C , 4nn	C	4.26	4.79
Va_C associate to X_C , 4nn	C	1.88	2.79
X_{Si}-Va_C pair			
Va_C exchange with X_{Si}	X	0*	0*
Va_C rotate X_{Si}	C	7.31	7.41
Va_C dissociate from X_{Si} , 2nn	C	6.02	6.06
Va_C associate to X_{Si} , 2nn	C	2.45	1.38
Va_C dissociate from X_{Si} , 3nn	C	5.70	4.29
Va_C associate to X_{Si} , 3nn	C	2.66	0.065

After the tracer diffusion coefficient of Cs was derived, the radiation-enhanced diffusion can be approximated by the following form:

$$D_{\text{Cs}}^{\text{rad}} = D_{\text{Cs}}^{\text{eq}} + x_{\text{V}}^{\text{rad}} \frac{D_{\text{Cs}}^{\text{eq}}}{x_{\text{V}}^{\text{eq}}}, \quad (2.2)$$

where $D_{\text{Cs}}^{\text{eq}}$ and x_{V}^{eq} are respectively the diffusion coefficient of Cs (Eq. 2.1) and vacancy concentration under the thermodynamic equilibrium condition, and $x_{\text{V}}^{\text{rad}}$ is the non-equilibrium vacancy concentration under irradiation. x_{V}^{eq} can be determined by the formation energy of a carbon vacancy, which is calculated to be between 4.18 eV (Si-rich) and 4.72 eV (C-rich). The excess vacancy concentration under irradiation can be calculated by the rate theory [27, 28, 5]

$$\frac{\partial x_{\text{V}}}{\partial t} = G + \frac{x_{\text{IV}}}{\tau_{\text{t}}} - k_{\text{rec}}(D_{\text{I}} + D_{\text{V}})x_{\text{I}}x_{\text{V}} - D_{\text{V}}x_{\text{V}}S_{\text{t}} - \frac{4\pi r_{\text{trap}}}{V_{\text{a}}} D_{\text{V}}x_{\text{V}}x_{\text{trap}} \quad (2.3)$$

$$\frac{\partial x_I}{\partial t} = G - k_{\text{rec}}(D_I + D_V)x_Ix_V - D_Ix_IS_t - \frac{4\pi r_{\text{trap}}}{V_a}D_Ix_Ix_{\text{tv}}, \quad (2.4)$$

where V and I denote vacancies and interstitials, respectively. Note that since the dominant point defects in SiC produced by irradiation are carbon vacancies and carbon interstitials [25], the evolution of other point defects, including silicon vacancies, silicon interstitials, and antisite defects, is not considered in the rate theory equations. $G = \xi K_0$ is the defect production rate, ξ is the displacement efficiency, and K_0 is the rate of radiation damage in terms of displacements per atom (dpa). $K_0 = \sigma_{\text{dpa}}\phi$, where σ_{dpa} is the dpa cross-section. k_{rec} is the coefficient of the recombination rate. Note that the recombination of a carbon interstitial and a carbon vacancy is not a spontaneous reaction but has a reaction barrier E_{rec} about 0.9 eV.

D_V and D_I in Eqs. 2.3 and 2.4 are respectively the diffusion coefficients of carbon vacancies and interstitials, r_{trap} is the trap recombination radius, x_{trap} is the trap density, and x_{tv} is the trapped vacancy concentration. S_t is the total sink strength, which includes the contributions of dislocations, GBs, and defect clusters

$$S_t = \rho_d + 3\frac{\sqrt{\rho_d}}{d_{\text{grain}}} + S_c, \quad (2.5)$$

where ρ_d is the dislocation density, d_{grain} is the grain size, and S_c is the sink strength from vacancy clusters, also called unstable matrix features. Interstitial clusters and dislocation loops, which can also be produced by irradiation, are not considered in this study. For the parameters used in the rate theory equations, please refer to the previous milestone report [5].

By making the following approximations $D_I \gg D_V$ and $D_Ix_I = D_Vx_V$, the steady-state solution of Eqs. 2.3 and 2.4 can be solved by finding roots of the polynomial. It will be numerically convenient to define the fraction of point defects that escape recombination to reach sinks as

$$g_s = \frac{x_V D_V S_t}{G}. \quad (2.6)$$

By placing Eq. 2.6 and the above two approximations into the steady-state condition of Eq. 2.3, g_s can be solved numerically. x_V can be derived by the relation with g_s in Eq. 2.6, and finally, the radiation-enhanced diffusion coefficient $D_{\text{Cs}}^{\text{rad}}$ can be calculated by Eq. 2.2.

Figure 2.1 shows the calculated radiation-enhanced diffusion coefficient of Cs, $D_{\text{Cs}}^{\text{rad}}$, in the bulk SiC, along with the calculated diffusion coefficient under thermodynamic equilibrium, $D_{\text{Cs}}^{\text{eq}}$. The difference between the blue and red lines in the plots of $D_{\text{Cs}}^{\text{eq}}$ and $D_{\text{Cs}}^{\text{rad}}$ is caused by the difference of carbon vacancy formation energy for C-rich and S-rich SiC. The calculation result of $D_{\text{Cs}}^{\text{rad}}$ shows that the transition from thermal diffusion to radiation-enhanced diffusion of via carbon vacancies happens at the temperature between ~ 1500 K and 2200 K. The blue and red $D_{\text{Cs}}^{\text{rad}}$ lines converge to a single line when the temperature is lower than ~ 1500 K, at which the Cs transport will be mostly mediated by the radiation-induced excess point defects instead of thermally activated vacancies at low temperatures. The result suggests that, similar to the transport of Ag, radiation-enhanced transport of Cs in SiC may still matter during the service condition of TRISO fuels. Note that the calculated $D_{\text{Cs}}^{\text{rad}}$ is still significant slower than the GB diffusivity, thus GB diffusion of Cs may still be the dominant transport mechanism.

It has been demonstrated in [5] that the binding energy of the vacancy cluster plays the most important role in the calculated excess vacancy concentration in SiC, which can further modify D_{Cs}^{rad} significantly. Figure 2.2 shows the calculated binding energies of vacancy clusters including different combinations of carbon and silicon vacancies. The result suggests the binding energy depends strongly on the number and type of vacancies in the cluster, and the mixed clusters, containing both carbon and silicon vacancies (green color in Figure 2.2), have a generally more pronounced binding than the clusters formed completely by carbon vacancies (blue color in Figure 2.2). The maximum binding energy reaches ~ 7 eV. The result also indicates that the effect of vacancy cluster on radiation-enhanced diffusion in SiC cannot be captured simply by a single binding energy. While the result presented in this section might still be a good approximation for high temperature where vacancy clusters are not as important as that at low temperature, a more comprehensive defect model that integrates molecular dynamics and cluster dynamics might be needed to address the complexity involved in the mixed defect cluster formation in SiC.

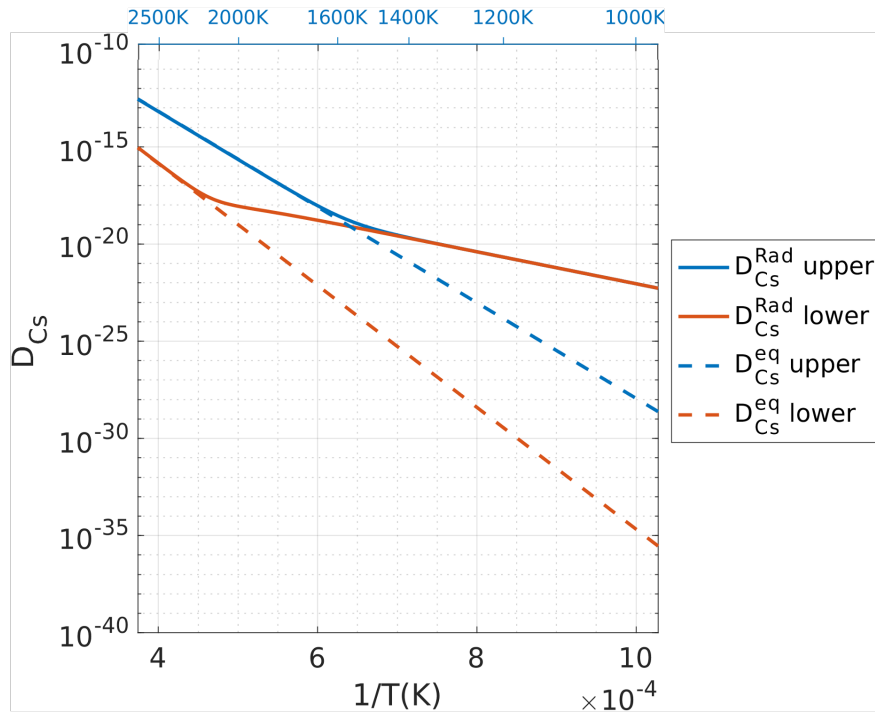


Figure 2.1. Plots showing the diffusion coefficient of Cs in bulk SiC as a function of reciprocal temperature. The solid blue and red lines show the calculated radiation-enhanced diffusion coefficient of Cs in bulk SiC under the AGR-1 conditions. The dashed lines are the thermal diffusion coefficient of Cs under thermodynamic equilibrium of the vacancy concentration.

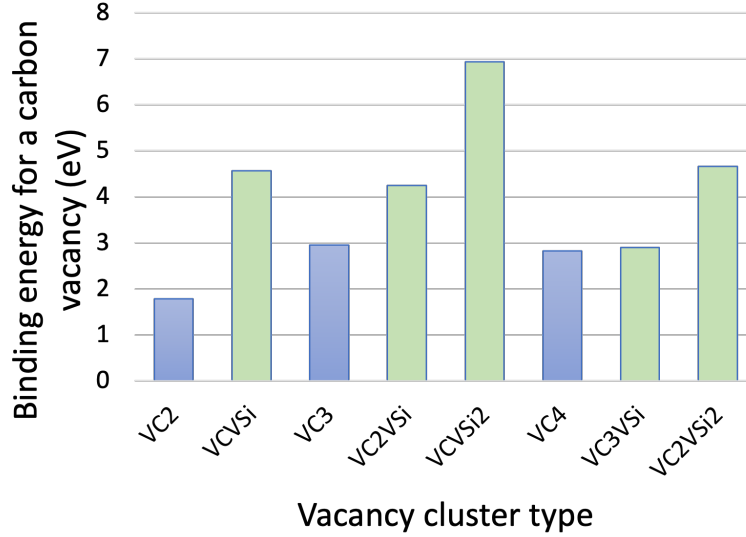


Figure 2.2. Binding energies of different vacancy clusters in SiC calculated by DFT. The green color indicates the mixed clusters, and the blue color indicates the carbon vacancy clusters.

2.2 Fitting the irradiation-enhanced Cs diffusivity in bulk SiC to be used at the mesoscale

Leveraging the Cs bulk diffusivity derived in Section 2.1 at the mesoscale requires fitting the results shown in Fig. 2.1 as a function of both temperature and neutron flux. In this work, we use the approach developed in Ref. [5], and Cs diffusivity in bulk SiC is therefore described as

$$D_{bulk}(T, F) = D^{th}(T) + D^{irr}(T, F) \quad (2.7)$$

with T the temperature in K, F the flux in $\text{n/m}^2/\text{s}$, $D^{th}(T)$ the diffusivity due to thermal effects in m^2/s , and $D^{irr}(T, F)$ the diffusivity due to irradiation effects in m^2/s . $D^{th}(T)$ is defined in Refs. [3, 4, 5] as

$$D^{th}(T) = D_0^{th} \exp\left(\frac{-Q^{th}}{RT}\right) \quad (2.8)$$

with $D_0^{th} = 4.7 \times 10^{-4} \text{ m}^2/\text{s}$ and $Q^{th} = 472 \times 10^3 \text{ J/mol}$. A Python script able to identify the change of slope due to irradiation-enhanced diffusivity from the Arrhenius law was then fitted to the low-temperature regime at different fluxes to determine $D^{irr}(T, F)$. The irradiation-enhanced bulk diffusivity is therefore defined as

$$D^{irr}(T, F) = D_0^{irr}(F) \left(\frac{-Q^{irr}(F)}{RT}\right), \quad (2.9)$$

where $D_0^{irr}(F)$ and $Q^{irr}(F)$ are functions of the neutron flux. $D_0^{irr}(F)$ increases with flux level as

$$D_0^{irr}(F) = a \left(\frac{F}{F_0} \right)^b, \quad (2.10)$$

where $F_0 = 1 \text{ n/m}^2/\text{s}$ ensures that F/F_0 is dimensionless, $b = 0.5051$ (-), and $a = 2.020 \times 10^{-23} \text{ m}^2/\text{s}$. The quality of this fit between $F = 4.7 \times 10^{13} \text{ n/m}^2/\text{s}$ and $F = 4.7 \times 10^{18} \text{ n/m}^2/\text{s}$, shown in Fig. 2.3a, is quantified by $R^2 = 1 - 2.8 \times 10^{-5}$. $Q^{irr}(F)$ is defined as

$$Q^{irr}(F) = c \ln(F) + d \quad (2.11)$$

with $c = 57.40 \text{ J/mol}$ and $d = 156188 \text{ J/mol}$. The quality of this fit between $F = 4.7 \times 10^{13} \text{ n/m}^2/\text{s}$ and $F = 4.7 \times 10^{18} \text{ n/m}^2/\text{s}$, shown in Fig. 2.3b, is quantified by $R^2 = 0.829$. Although the fit is not perfect, we attribute the departures from the fit to numerical fluctuations, and point out that the total variations in $Q^{irr}(F)$ are quite limited, and most of the flux dependencies are captured in $D_0^{irr}(F)$.

The resulting fit for $D^{irr}(T, F)$ is shown in Fig. 2.3c. The fit of the bulk diffusion proposed in this section accurately captures the two different regimes (i.e., the thermal diffusion at higher temperatures and the irradiation-enhanced diffusion at lower temperatures). This fit will be used in the rest of this manuscript to describe the irradiation-enhanced Cs diffusion in bulk SiC.

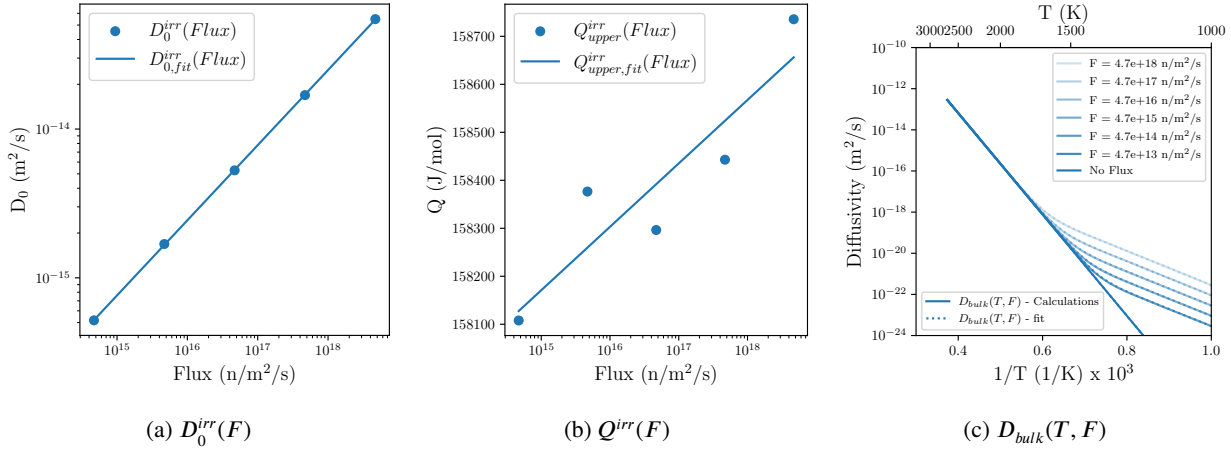


Figure 2.3. Fitting the irradiation-enhanced bulk Cs diffusion as a function of flux. (a) shows how D_0^{irr} evolves with the flux and how it was fitted using Eq. (2.10), and (b) shows how Q^{irr} evolves with the flux and how it was fitted using Eq. (2.11). (c) shows the final fit for $D_{bulk}(T, F)$ described in Eq. (2.7).

3. DETERMINATION OF GB Cs DIFFUSIVITY IN SiC

Classical molecular dynamics (MD) simulations have been performed using the LAMMPS code [29] to study Cs diffusion along SiC GBs. Due to the lack of empirical potential for the SiC-Cs system in the literature, we have developed one in FY-23 using the analytical bond-order potential (ABOP) formalism [30] by fitting to the DFT-calculated formation energies of Cs in SiC. A new potential for the SiC+Ag system has also been developed using the same formalism. As shown in Figure 3.1, the ABOP potential can reasonably reproduce DFT results for both Cs and Ag. It is worth noting here that the very high formation energies of Cs (Figure 3.1a) would suggest its extremely low solubility in bulk SiC under equilibrium conditions. This is consistent with the much larger radius of Cs (3.43 Å) than those of Si (2.1 Å) and C (1.7 Å). Compared with Cs, Ag has much smaller formation energies in SiC (Figure 3.1b), which is again consistent with its much smaller radius (1.72 Å) than Cs.

Figure 3.2 illustrates the simulation cell for the $\Sigma 5$ (210)/[001] GB of SiC. Here, the X-axis is parallel to the GB tilt axis, while the Y-axis is parallel to the GB period. The Z-axis is perpendicular to the GB plane. Figure 3.3 reports the MD-calculated mean-squared displacement (MSD) data for both Cs and Ag atoms from t=0 ns to 10 ns. The MSD results show that Cs diffusion is at least one order of magnitude slower than Ag, which may be explained by the significantly larger size of Cs than Ag. It can also be concluded that there is negligible diffusion of Cs and Ag atoms away from the GB plane (Figures 3.3e and 3.3f).

Through a linear fitting of the MSD vs. time data, the diffusivities of Cs and Ag along the $\Sigma 5$ (210)/[001] GB of SiC can be calculated using the Einstein relation, and the results are reported in Figure 3.4. By fitting the MD results for Cs and Ag to the Arrhenius equation, we have obtained the following equations to describe the average diffusivity along X and Y directions within the GB plane for Cs and Ag

$$D_{Cs} = 4.05 \times 10^{-11} \exp \left(-\frac{0.525}{k_B T} \right), \quad (3.1)$$

$$D_{Ag} = 2.37 \times 10^{-9} \exp \left(-\frac{0.830}{k_B T} \right), \quad (3.2)$$

where k_B is the Boltzmann constant.

In this work, we have further performed MD simulations to predict the diffusivities of Cs and Ag along random HAGBs in SiC. The details of constructing the polycrystalline SiC samples can be found in the previous milestone

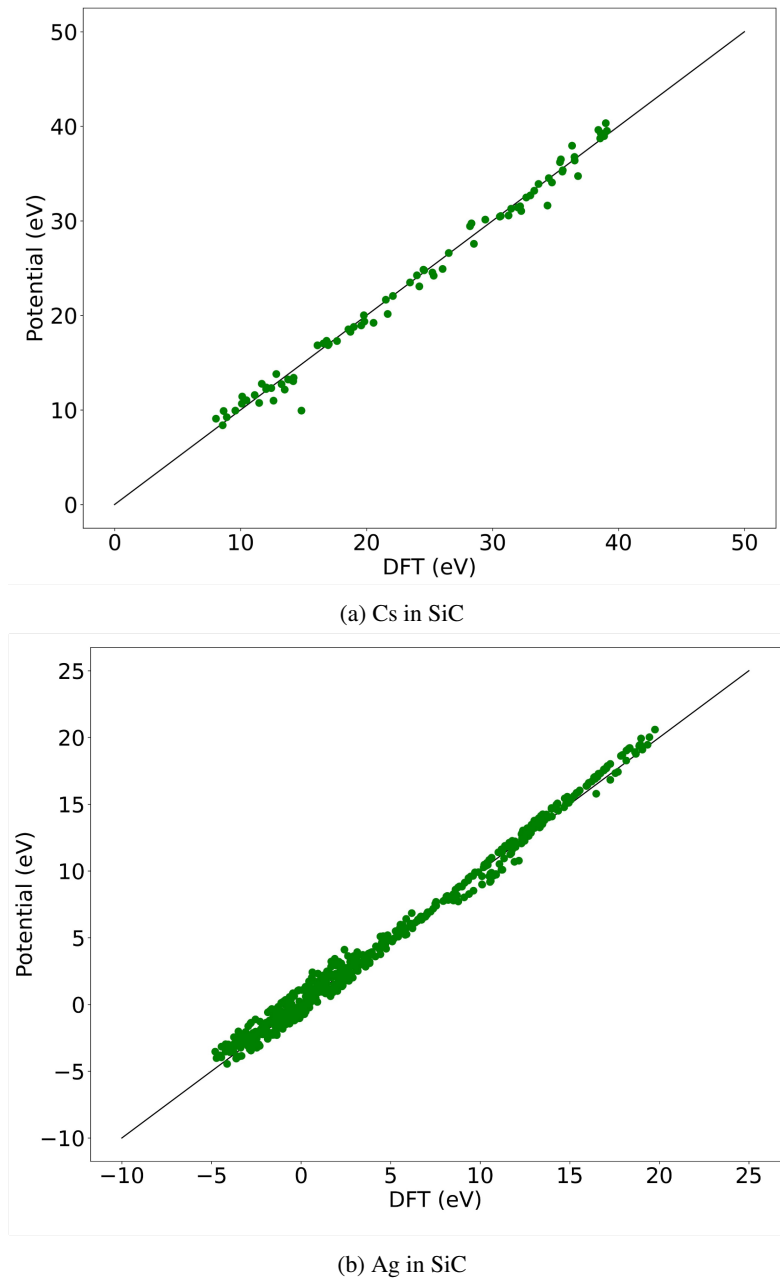


Figure 3.1. Comparison between DFT-calculated and ABOP-calculated formation energies of Cs and Ag in SiC. The solid lines represent perfect agreement between DFT and new empirical potentials developed in this work.

report [3]. The diffusivities calculated from the MD simulations are shown in Figure 3.5. Interestingly, contrary to our previous assumption that random GBs in SiC provide the fastest diffusion paths for fission products to escape TRISO particles [3], the present MD simulations suggest that diffusion along $\Sigma 5$ GB may actually be faster than along random

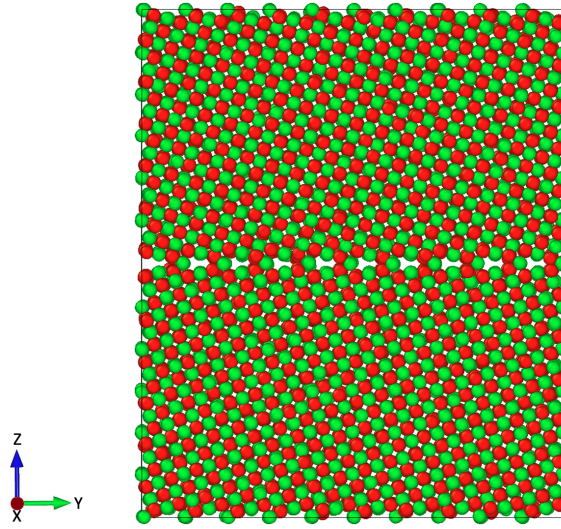


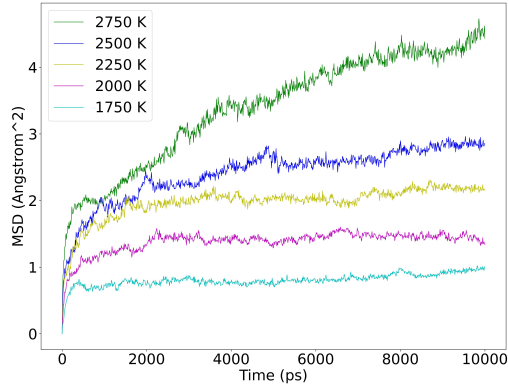
Figure 3.2. $\Sigma 5$ (210)/[001] GB of SiC. The green and red spheres represent Si and C atoms, respectively.

GBs for both Cs and Ag. In future studies, long-time MD simulations with more accurate empirical potentials can be performed to confirm this finding.

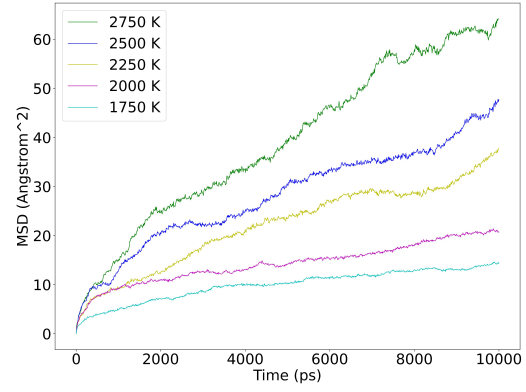
The following equations can be used to estimate the average diffusivities of Cs and Ag along the random HAGBs in SiC:

$$D_{Cs} = 3.88 \times 10^{-11} \exp \left(-\frac{0.697}{k_B T} \right) \quad (3.3)$$

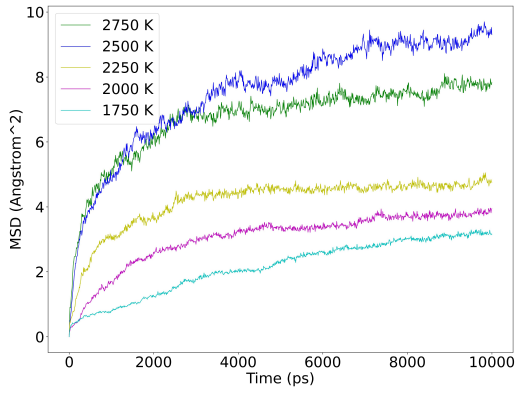
$$D_{Ag} = 9.31 \times 10^{-11} \exp \left(-\frac{0.837}{k_B T} \right). \quad (3.4)$$



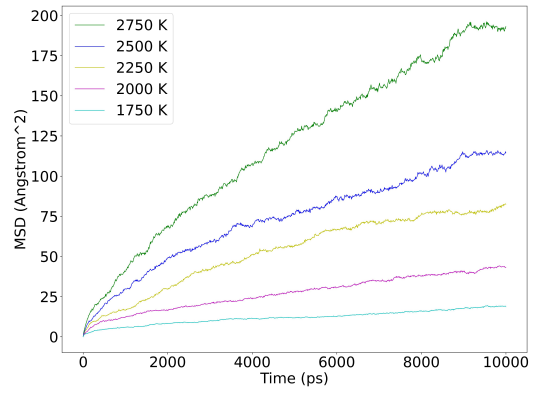
(a) MSD for Cs along X-axis



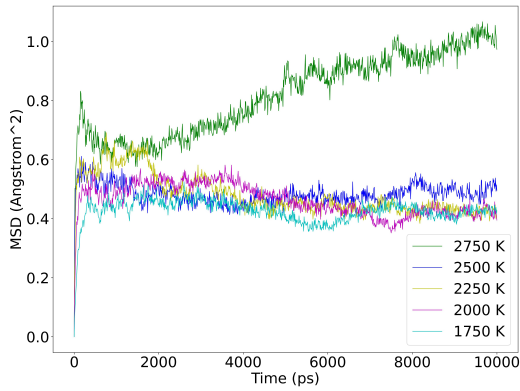
(b) MSD for Ag along X-axis



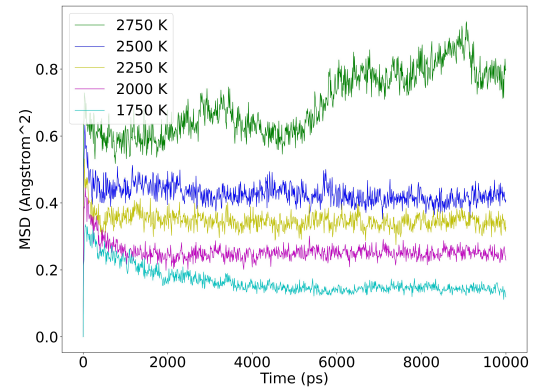
(c) MSD for Cs along Y-axis



(d) MSD for Ag along Y-axis



(e) MSD for Cs along Z-axis



(f) MSD for Ag along Z-axis

Figure 3.3. MSD data for Cs and Ag atoms diffusing within the $\Sigma 5$ (210)/[001] GB of SiC at various temperatures.

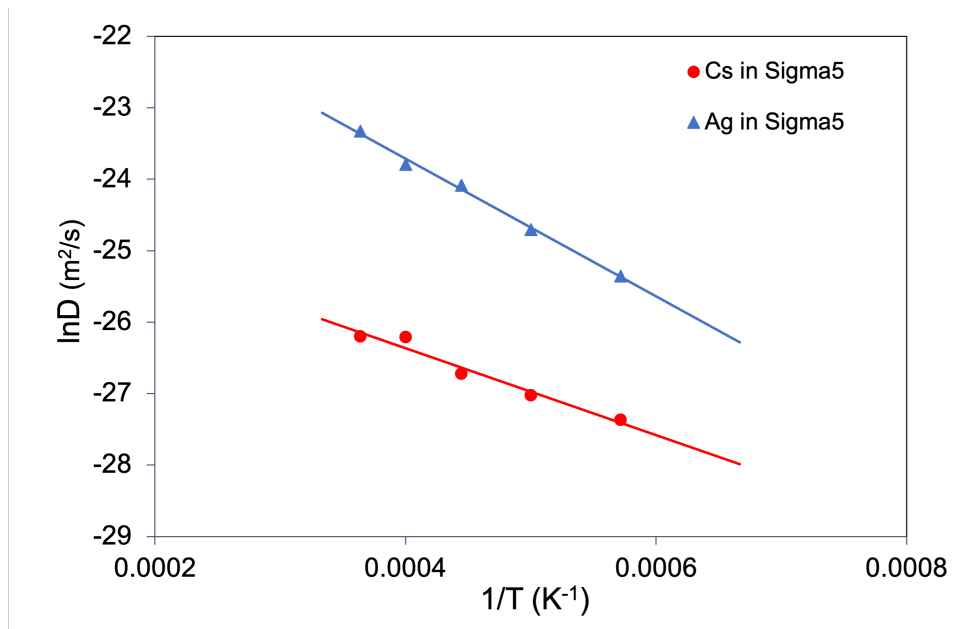
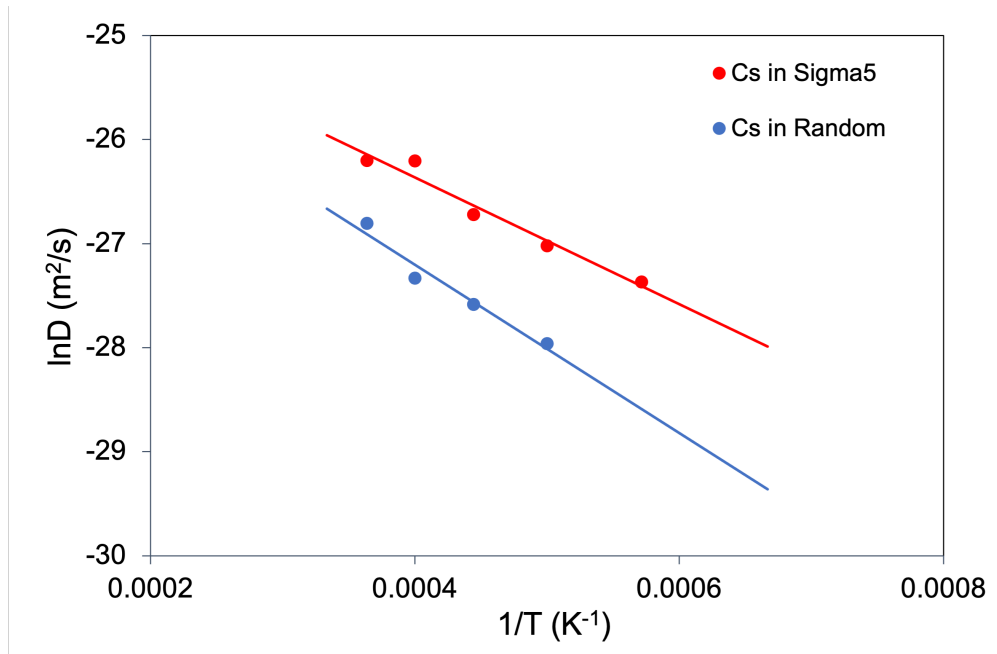
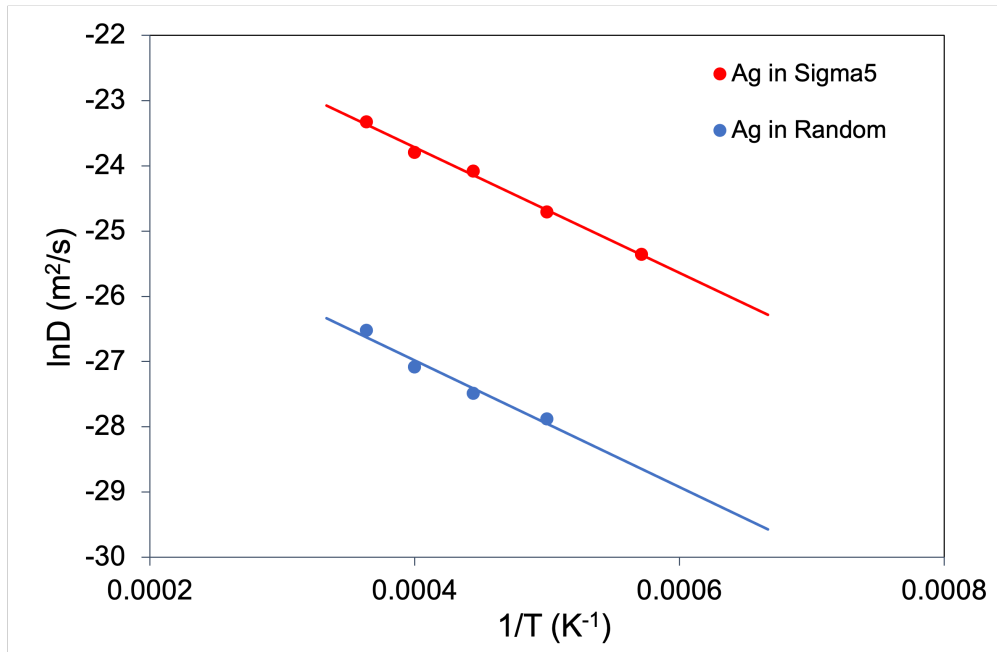


Figure 3.4. Arrhenius plot for Cs and Ag diffusivities within the $\Sigma 5$ (210)/[001] GB of SiC. The solid lines represents the best fitting of MD data using the Arrhenius equation.



(a) Cs in SiC



(b) Ag in SiC

Figure 3.5. Arrhenius plot for Cs and Ag diffusivities within the random HAGBs of SiC. Results for $\Sigma 5$ (210)/[001] GB are also shown for comparison. The solid lines represents the best fitting of MD data using the Arrhenius equation.

4. DEVELOPMENT AND VALIDATION OF A MESO-SCALE EFFECTIVE Cs DIFFUSIVITY IN SiC

In this section, we develop and validate a effective Cs diffusivity model at the mesoscale based on the atomistic results provided in Sections 2 and 3. We first detail in Section 4.1 the microstructures used to represent the polycrystalline nature of the SiC layer and how they were generated. In Section 4.2, we detail the numerical method used to determine the effective diffusivity at the mesoscale and specify the temperature and neutron flux ranges for which the model was developed. The results of this approach are described in Section 4.3, and the results are then compared to experimental values and other computational efforts. To better correspond to experimental data, a change is made to the approach in Section 4.4, and the resulting diffusivity is once again compared to experimental data, exhibiting a higher accuracy.

4.1 Description of the SiC microstructures

The mesoscale simulations were performed in a similar fashion and with the same polycrystalline structures as in Refs. [3, 4, 5]. These microstructures were generated using the approach and script described in Ref. [31, 32]. They are 20 2D domains of dimensions $9 \mu\text{m} \times 9 \mu\text{m}$ generated with the desired grain sizes, grain aspect ratios, and GB widths. Their grain major axis ranges from $0.75 \mu\text{m}$ to $3 \mu\text{m}$, and the grain minor axis ranges from $0.3 \mu\text{m}$ to $0.82 \mu\text{m}$ to correspond to grain sizes measured from AGR-1 and AGR-2 SiC layers [33]. Although the GB size of the polycrystalline SiC is approximately equal to 1 nm , with variations between HAGBs and low-angle grain boundary (LAGB)s, the GB width is scaled up to 60 nm using the approach described in Refs. [3, 4] to limit computational costs while minimizing computational errors. As mentioned above, the simulated microstructures cover the variations in grain dimensions found in the AGR-1 and AGR-2 fuel batches, hence providing results relevant for realistic SiC grain sizes for TRISO fuel particles.

As in Refs. [3, 4, 5], the polycrystalline structures used in this section have continuous interfaces described using a set of N continuous order parameters η_{Gr_i} with $i \in [1, N]$ [34]. A given order parameter is equal to 1 in a given grains, and equal to 0 in neighboring grains, with a continuous transition from 1 to 0 at the GB. The GBs are described by

$$\chi = \sum_i^N \eta_{Gr_i}^2, \quad (4.1)$$

where χ is equal to 1 in the grain interior and continuously transitions to 0.5 along the mid plane of the GBs. Based on this continuous description of the grain structure, the diffusion coefficient is defined as

$$D = (1 - h_{GB})D_b + h_{GB}D_{GB} \quad (4.2)$$

with D_b defined in Chapter 2 and D_{GB} defined in Chapter 3. h_{GB} is defined as

$$h_{GB}(\chi) = 1 - \frac{1}{2} \left(1.0 + \tanh \left((\chi - \chi_0) \frac{2 \tanh^{-1}(0.8)}{\Delta} \right) \right) \quad (4.3)$$

with χ_0 the point at which $h_{GB}(\chi_0) = 0.5$ and Δ the interfacial width, that is, the distance $|\chi_{0.9} - \chi_{0.1}|$ for $h_{GB}(\chi_{0.1}) = 0.1$ and $h_{GB}(\chi_{0.9}) = 0.9$. This specific interpolation function was used to ensure that the diffusion was the same everywhere in the GBs, including at triple junctions [3, 4, 5]. As discussed in [3, 4], other common interpolation functions are often equal to values lower than 1 at triple junctions, which artificially slow down diffusion. The parameters χ_0 and Δ need to be selected to maximize Δ (i.e., the smoothness of the slope) while ensuring $|h_{GB}(0.5) - 1| \leq \epsilon_{GB}$ and $|h_{GB}(1) - 0| \leq \epsilon_{bulk}$ [5]. The tolerances ϵ_{GB} (tolerated error in the GBs) and ϵ_{bulk} (tolerated error in the bulk) need to be defined as a function of the ratio of bulk and GB diffusivities. The local diffusivity D defined in Eq. (4.2) should be equal to D_b in the bulk and equal to D_{GB} at GBs. In the bulk, this leads to $\epsilon_{bulk} \ll D_b/D_{GB}$ and $\epsilon_{bulk} \ll 1$. At GBs, this translates into $\epsilon_{GB} \ll D_{GB}/D_b$ and $\epsilon_{GB} \ll 1$. Given the expressions provided in Chapter 2 and D_{GB} defined in Chapter 3, we can reasonably use $\epsilon_{bulk} = 10^{-15}$ and $\epsilon_{GB} = 10^{-2}$. This leads to $\chi_0 = 0.625$ and $\Delta = 0.0477$.

4.2 Method for effective diffusivity calculations

As in Refs. [3, 4, 5], we use the asymptotic expansion homogenization (AEH) method described in Ref. [35] to determine the effective diffusivity coefficient at the mesoscale. This method is already implemented in Multiphysics Object Oriented Simulation Environment (MOOSE) [36, 37, 38], making it possible to determine effective material properties in a domain with periodic boundary conditions. In the current work, the polycrystals were created with periodic boundary conditions, and the temperature is considered constant across the entire domain. This method can therefore be applied. Simulations are performed for all 20 microstructures with temperatures ranging from 1000 K to 2400 K with 200 K increments. In the simulations presented in this work, the flux equals 0, 4.7×10^{13} n/m²/s, and then every order of magnitude up to 4.7×10^{18} n/m²/s. This covers a wide range of temperatures and flux around the relevant AGR-1 and AGR-2 operation conditions [39].

Note that in this report, we develop two mesoscale models: one using the bulk and $\Sigma 5$ diffusivities and one using the bulk and HAGB diffusivities. A model which combined all diffusivities from different GB types is being developed in parallel and is detailed in Chapter 7 for Ag. The same approach will be used in future work for Cs. In the meantime, the two models provide bounding values.

4.3 Effective diffusivity calculations

The results of the simulations performed for the microstructures and irradiation conditions described in Section 4.2 are shown in Fig. 4.1. This figure shows the bulk diffusivity derived in Chapter 2, including irradiation effects, the GB diffusivities for $\Sigma 5$ and HAGB GBs, and the resulting effective diffusivity for different temperatures, grain sizes, and neutron fluxes. It is interesting to note that at higher temperatures, the effective diffusivity approaches the bulk diffusivity, supporting the hypothesis that while GB diffusivity is significantly higher than bulk diffusivity, the difference is smaller at higher temperatures, and diffusivity is dominated by the medium representing the larger volume (i.e., the bulk). At lower temperatures, however, effective diffusivity becomes much higher than bulk diffusivity, and the activation energy seems to become similar to that of GB diffusivity.

The mesoscale calculations results can be fitted to obtain a temperature, irradiation, and grain size dependent effective Cs diffusivity in SiC to be used in fuel performance codes. The approach used is based on the one developed in Refs. [3, 4, 5], where the total effective Cs diffusivity in SiC is defined as

$$D^{eff,tot}(T, F, m_i, m_a) = D_{bulk}(T, F) + D^{eff,th}(T, m_i, m_a) + D^{eff,irr}(T, F, m_i, m_a), \quad (4.4)$$

with T the temperature, F the irradiation flux, m_i and m_a the minor and major axis lengths, respectively, $D_{bulk}(T, F)$ the bulk diffusivity defined in Eqs. (2.7) to (2.11), $D^{eff,th}(T, m_i, m_a)$ the thermal contribution to effective diffusion,

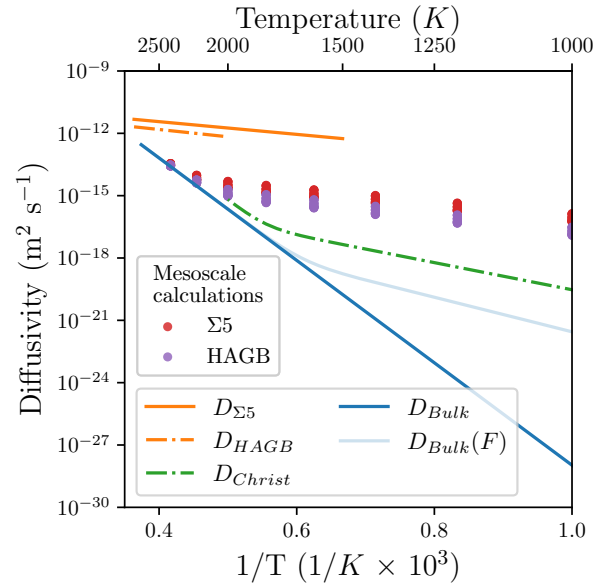


Figure 4.1. Comparison of the bulk and GB diffusivities with the empirical fit from Christ [21] used in BISON, and the data points obtained from the mesoscale simulations. The red dots show the effective diffusivities obtained when assuming that all GBs are diffusing as $\Sigma 5$ GBs; the purple dots show the effective diffusivities obtained when assuming that all GBs are diffusing as HAGBs.

and $D^{eff,irr}(T, F, m_i, m_a)$ the contribution from irradiation-enhanced diffusivity.

As opposed to the expression developed in Refs. [3, 4, 5], Eq. (4.4) includes $D_{bulk}(T, F)$ to model the bulk dominated regime at high temperatures. The steps developed in Refs. [3, 4, 5] required to develop this model and determine $D^{eff,th}(T, m_i, m_a)$ and $D^{eff,irr}(T, F, m_i, m_a)$ are:

1. **Bulk-dominated regime fit:** At higher temperatures ($T > 2000$ K), effective diffusivity is dominated by bulk diffusivity, and no additional effect (grain size, irradiation) is appreciable.
2. **Thermal fit for ($T \leq 2000$ K):** Fit the thermal diffusivity as a function of temperature for each microstructure using simulations without irradiation.
3. **Microstructure-dependent fit for ($T \leq 2000$ K):** Fit the pre-exponential factor and the energy barrier of the thermal diffusivity as a function of grain size using simulations without irradiation.
4. **Irradiation-dependent fit for ($T \leq 2000$ K):** With thermal diffusion now fitted as a function of temperature and grain size, focus on irradiation effects, which are expected to depend on temperature, irradiation levels, and grain size.

To fit thermal diffusivity below 2000 K, the temperature-dependent effective diffusivity obtained for each microstructure is fitted to an Arrhenius equation to obtain a pre-exponential factor D_0 and an energy barrier Q for each polycrystal. These coefficients are presented in Fig. 4.2, where they are described as functions of grain major and minor axis length. As in Refs. [3, 4, 5], we found that the grain major axis length does not have a significant influence on D_0 or Q . However, both can be described as linearly dependent on the grain minor axis length. The faster diffusivity for smaller minor axis grains is attributed to a higher density of GBs to diffuse radially through the SiC polycrystalline structure, therefore increasing the effective diffusivity of the SiC layer. This is extensively discussed in Refs. [3, 4, 5].

The thermal contribution to the effective Cs diffusivity in SiC as a function of temperature (from 1000 K to 2000 K) and grain size (minor axis from 0.3 μm to 0.82 μm) can therefore be described as

$$D^{eff,th}(T, m_i) = (D_{m,0} + m_i D_{m,1}) \exp\left(-\frac{Q_{m,0} + m_i Q_{m,1}}{RT}\right) \quad (4.5)$$

with T in Kelvin, $R = 8.315$ J/K/mol, and m_i in μm . The numerical values for the parameters $D_{m,0}$, $D_{m,1}$, $Q_{m,0}$, and $Q_{m,1}$ are provided in Table 4.1.

The irradiation-enhanced contribution to the effective diffusivity is shown in Fig. 4.3 and can be described as

$$D^{eff,irr}(T, F, m_i) = D^{eff,th}(T, m_i) C^{irr}(T, F, m_i), \quad (4.6)$$

with $D^{eff,th}$ from Eq. (4.5) and C^{irr} an adimensional temperature, flux, and minor grain axis dependent coefficient defined as

$$C^{irr}(T, F, m_i) = c_0^{irr} \left(\frac{F}{F_0}\right)^{c_1^{irr}} (1 + c_2^{irr} m_i) \exp\left(\frac{c_3^{irr}}{T}\right), \quad (4.7)$$

with $F_0 = 1$ n/m²/s ensuring that F/F_0 is adimensional. C^{irr} is therefore linearly dependent on the grain minor axis length, increases exponentially with the inverse of the temperature, and evolves as a power law with respect to the flux. Note that, just like $D^{eff,th}(T, m_i)$, $D^{eff,irr}$ is independent of the grain major axis length, which is visible in

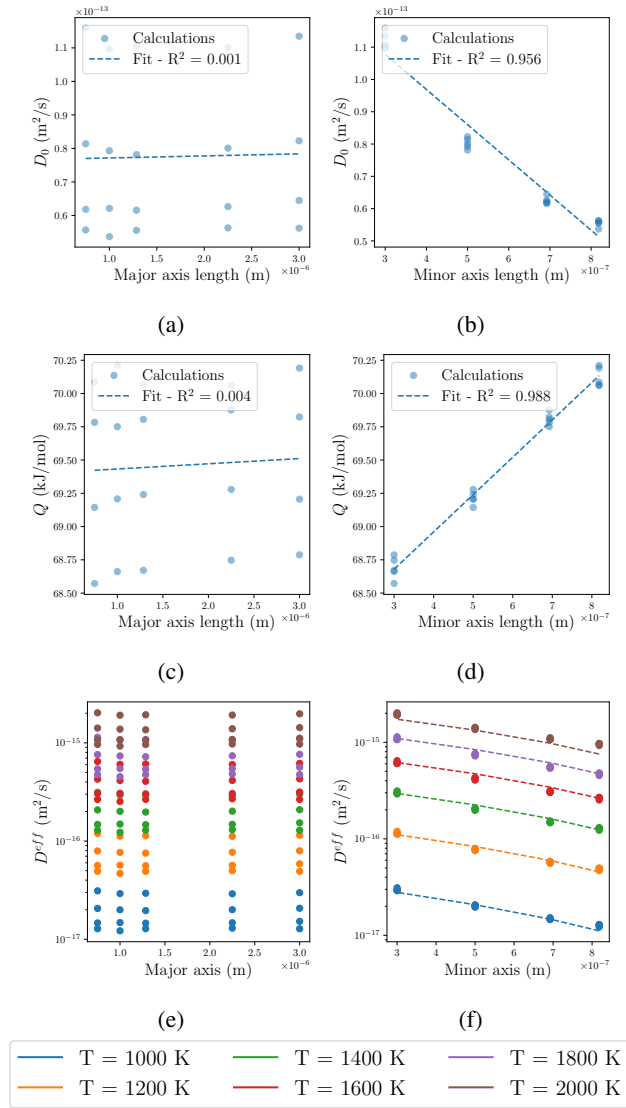


Figure 4.2. Derivation of the thermal contribution to the effective Cs diffusion coefficient as a function of the temperature T , the grain minor axis length m_i , and the grain major axis length m_a . These results assume that all the GBs diffuse like HAGBs, but similar trends and values are obtained for $\Sigma 5$ GBs. (a,b) show how D_0 depends on (a) m_a and (b) m_i , and (c,d) show how Q depends on (c) m_a and (d) m_i . (e,f) show how the thermal contribution to the effective diffusion coefficient $D^{eff,th}$ depends on (e) m_a and (f) m_i for different temperatures. The best fit, which successfully captures the temperature and microstructure effects on $D^{eff,th}$, is shown in (f).

Fig. 4.3. The numerical values for the parameters are provided in Table 4.1. Although irradiation effects are visible in Fig. 4.3, it does not significantly affect the effective diffusivity. This is because in the current model, irradiation effects on bulk diffusivity only are considered, and they are significant only at low temperatures, when GB diffusivity clearly dominates transport.

Table 4.1. Parameter values for the mesoscale effective diffusion described in Eqs. (4.4) to (4.7).

Equation	Parameter	Value	Units
Effective diffusivity with $\Sigma 5$ GBs			
Eq. (4.5)	$D_{m,0}$	2.057×10^{-13}	m^2s^{-1}
	$D_{m,1}$	-1.696×10^{-7}	ms^{-1}
	$Q_{m,0}$	58.8×10^3	J/mol
	$Q_{m,1}$	1.193×10^9	J/mol/m
Eq. (4.7)	c_0^{irr}	3.459×10^{-11}	$(\text{n/m}^2/\text{s})^{-1}$
	c_1^{irr}	0.501	(-)
	c_2^{irr}	4.87×10^6	m^{-1}
	c_3^{irr}	-10.6×10^3	K^{-1}
Effective diffusivity with HAGBs			
Eq. (4.5)	$D_{m,0}$	1.405×10^{-13}	m^2s^{-1}
	$D_{m,1}$	-1.090×10^{-7}	ms^{-1}
	$Q_{m,0}$	67.8×10^3	J/mol
	$Q_{m,1}$	2.807×10^9	J/mol/m
Eq. (4.7)	c_0^{irr}	3.219×10^{-11}	$(\text{n/m}^2/\text{s})^{-1}$
	c_1^{irr}	0.501	(-)
	c_2^{irr}	4.00×10^6	m^{-1}
	c_3^{irr}	-8.50×10^3	K^{-1}

The effective Cs diffusivity in SiC is defined in Eqs. (4.4) to (4.7). This expression explains the two temperature regimes as a transition from bulk-dominated to GB-dominated diffusion and quantifies for temperature (from 1000 K to 2000 K), grain size (minor axis from $0.3 \mu\text{m}$ to $0.82 \mu\text{m}$), and irradiation effects (0 to $4.7 \times 10^{18} \text{ n/m}^2/\text{s}$). Although irradiation effects are not significant at the mesoscale, the grain size effect is clearly visible in Fig. 4.4. As shown in Fig. 4.4, $D^{eff,tot}(T, F, m_i)$ exhibits similar temperature regimes and activation energies as the empirical value proposed by Christ [21]. It overestimates the value from Ref. [21], but the discrepancy falls within the scatter shown in Fig. 1.1. Nevertheless, the next section focuses on slightly modifying this approach to obtain better agreement with the data from Ref. [21].

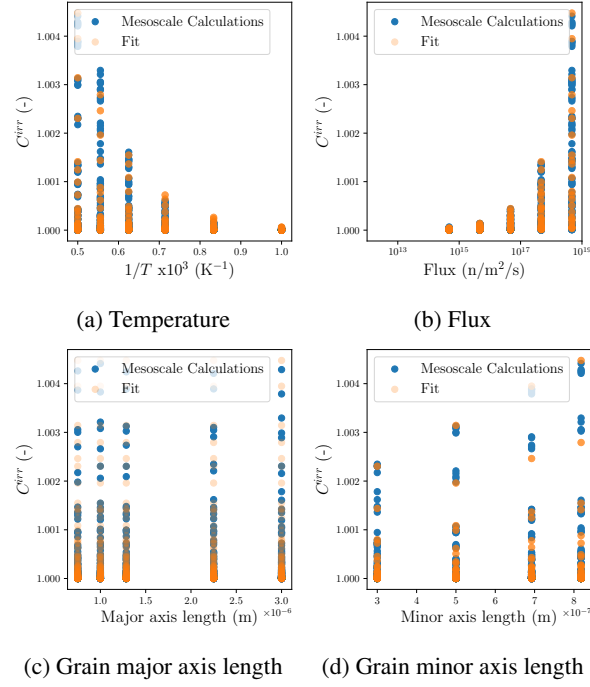


Figure 4.3. Influence of (a) temperature, (b) irradiation flux, and (c,d) grain major and minor axis lengths on the irradiation-enhanced diffusion contribution— C^{irr} from Eq. (4.7)—in polycrystalline SiC microstructures. These results assume that all the GBs diffuse like HAGBs, but similar trends and values are obtained for $\Sigma 5$ GBs. The effect of temperature, flux, and grain minor axis length is accurately captured in Eq. (4.6), as shown by the match between data points from mesoscale calculations and the model's predictions.

4.4 Improvement of the Cs effective diffusivity calculations

As noted in Fig. 4.4, the current multiscale approach slightly overestimates the empirical diffusivity from Ref. [21]. Since uncertainty is associated with the bulk and GB diffusivities derived in Chapters 2 and 3, we aim to modify these values to obtain an effective diffusivity that matches with the empirical diffusivity. Since the bulk-dominated regime at higher temperatures is already well predicted in Fig. 4.4, we kept the same bulk diffusivity values. However, the HAGB diffusivity is decreased until low temperature diffusivity better match the empirical diffusivity. To achieve these results, we have found that dividing the pre-exponential factor of the HAGB diffusivity by 100 provides satisfying results. Except for this change, the simulations are performed just as in Section 4.2, and the analysis follows the same procedure as detailed in Section 4.3. The updated results are shown in Figs. 4.5 to 4.7 and Table 4.2.

The updated mesoscale model for effective Cs diffusivity in SiC, which assumes that the HAGB diffusivity is 100 times smaller than derived in Chapter 3, better matches the empirical diffusivity from Ref. [21]. As shown in Fig. 4.7, the effective diffusivity developed in this work explains the temperature regimes experimentally observed by a transition from a bulk to a GB-dominated diffusion. The transition temperature is also accurately predicted around 1800 K, and the activation energies of the two regimes are similar to the ones of the empirical fit. This is the first modeling approach

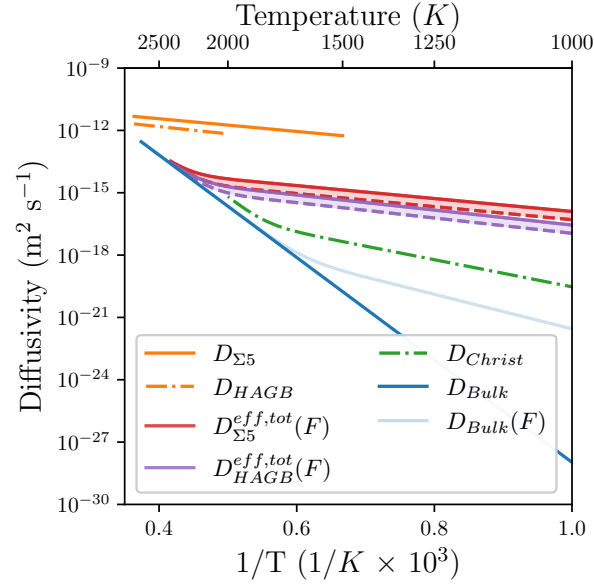


Figure 4.4. Comparison of the Cs diffusion coefficients provided by atomistic simulations (i.e., the temperature and irradiation-dependent bulk D_{bulk} derived in Chapter 2 and the GB D_{GB} Chapter 3), the empirical coefficient D_{Christ} used in BISON [21], and the mesoscale effective diffusivity models from the current study $D^{eff,tot}$ (Eqs. (4.4) to (4.7)). $D_{\Sigma 5}^{eff,tot}$ and $D_{HAGB}^{eff,tot}$ assume that all the GBs are $\Sigma 5$ or HAGB GBs, respectively. The range between the full and dotted lines for $D^{eff,tot}$ correspond to extreme grain minor axis length values of the SiC microstructures described in Section 4.1.

Table 4.2. Parameter values for the mesoscale effective diffusion described in Eqs. (4.4) to (4.7) but with the HAGB diffusivity reduced by a factor of 100.

Equation	Parameter	Value	Units
Eq. (4.5)	$D_{m,0}$	1.315×10^{-15}	$\text{m}^2 \text{s}^{-1}$
	$D_{m,1}$	-1.077×10^{-9}	ms^{-1}
	$Q_{m,0}$	67.5×10^3	J/mol
	$Q_{m,1}$	1.289×10^9	J/mol/m
Eq. (4.7)	c_0^{irr}	7.407×10^{-9}	$(\text{n/m}^2/\text{s})^{-1}$
	c_1^{irr}	0.498	(-)
	c_2^{irr}	5.405×10^6	m^{-1}
	c_3^{irr}	-10.17×10^3	K^{-1}

known to the authors to explain this phenomenon and confirm the hypothesis formulated in Chapter 1. In addition to this physical insight, the main advantages of the multi-scale approach presented in this work are that it quantifies the effect of grain size, as well as the seemingly minimal effect of irradiation enhanced diffusivity in bulk SiC.

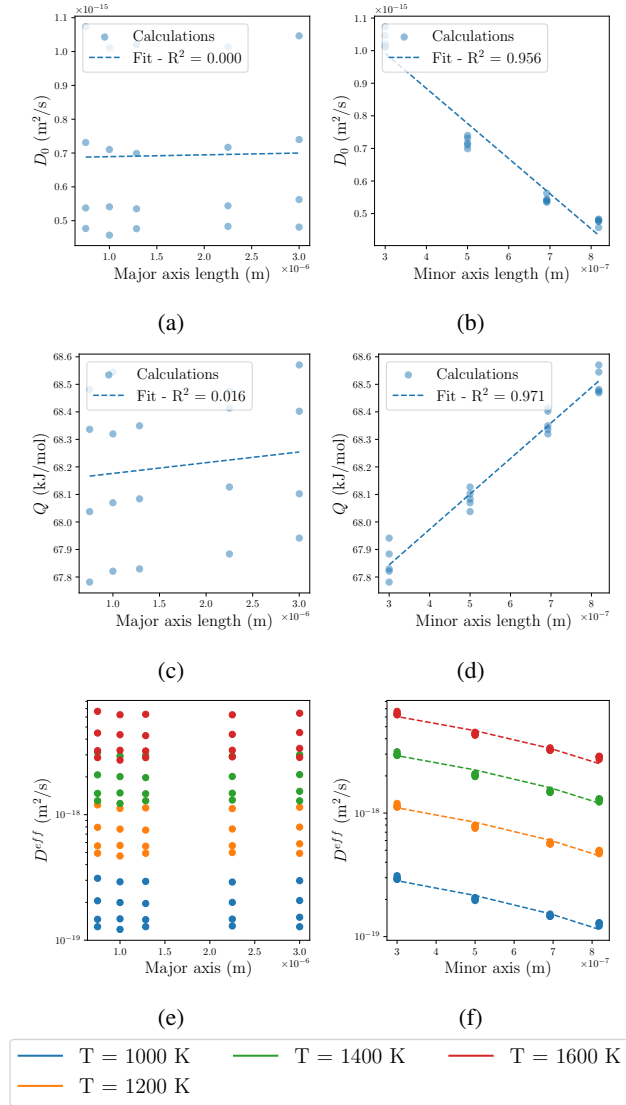


Figure 4.5. Derivation of the thermal contribution to the effective Cs diffusion coefficient as a function of the temperature T , the grain minor axis length m_i , and the grain major axis length m_a with a reduced HAGB diffusivity. This figure is the equivalent of Fig. 4.2 but with a HAGB diffusivity divided by 100.

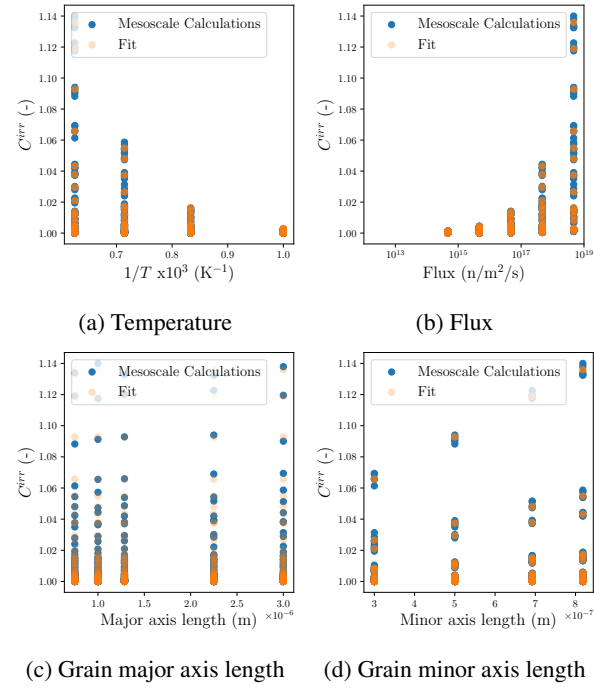


Figure 4.6. Influence of (a) temperature, (b) flux, and (c,d) grain major and minor axis lengths on the irradiation-enhanced diffusion contribution (C^{irr} from Eq. (4.7)) in polycrystalline SiC microstructures, with a reduced HAGB diffusivity. This figure is the equivalent of Fig. 4.3 but with a HAGB diffusivity divided by 100. The trends and conclusion remain similar.

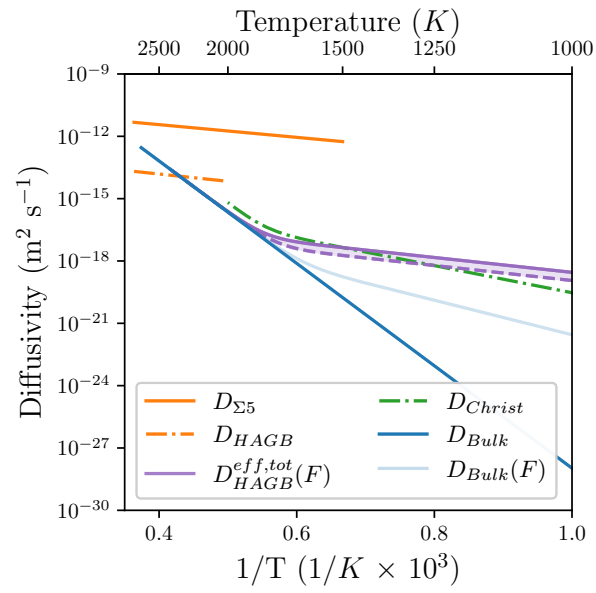


Figure 4.7. Comparison of the atomistic and modified effective diffusivities with the empirical model from Ref. [21]. The modified effective diffusivity model is similar to the model presented in Fig. 4.7, but with a HAGB diffusivity divided by 100. The modified diffusivity better matches the empirical model.

5. VALIDATION OF THE EFFECTIVE Cs DIFFUSIVITY IN SiC USING AGR-1 AND AGR-2 DATA

The effective Cs diffusivity derived in the previous section has been implemented in the fuel performance code BISON. The resulting predictions, compared to the ones using the existing empirical diffusivity from Christ [21], show the effect of microstructure and irradiation levels on Cs release from TRISO particles. The results are shown in Fig. 5.1, along with the experimental data. Note that the grain size used for these simulations correspond to the measurements from [33] and are listed in Table 5.1 for the relevant compacts.

Table 5.1. Microstructure properties of AGR-1 and AGR-2 fuel capsules obtained from cross-referencing Ref. [33] and Table 6 from Ref. [40]. Optimized values are determined by comparing model's predictions against PIE data.

AGR campaign	AGR-1						AGR-2		
Compact	1-3-1	3-2-1	4-1-1	4-4-2	5-3-1	6-1-1	6-3-3	3-3-1	2-2-2
Fuel variant	V3	B	V3	V3	V1	B	UCO	UO ₂	UCO
Min grain minor axis size (μm)	0.23	0.41	0.23	0.23	0.55	0.41	0.30	0.39	0.30
Max grain minor axis size (μm)	0.39	0.84	0.39	0.39	0.81	0.84	0.40	0.51	0.40
Optimized grain minor axis size (μm)	0.39	0.82	0.39	0.39	0.81	0.76	0.30	0.39	0.40

As shown in Fig. 5.1, using the effective diffusivity developed by the work detailed in the previous sections—see Eqs. (4.4) to (4.7) and Table 4.2 in Section 4.4—improves the BISON predictions for all compacts. Improvement for AGR-1 compact is significant (orders of magnitude). As with Ag release [3, 4, 5], the multi-scale, mechanistic approach developed through the NEAMS program has improved BISON predictions of Cs release.

Note that the grain size effect on diffusion described and quantified in Sections 4.3 and 4.4 significantly impacts fission product release. The range provided for the mesoscale BISON predictions in Fig. 5.1 correspond to the grain size variation experimentally measured in the SiC layer of AGR fuel. These results suggest that manufacturing TRISO particles with thick SiC grains in the direction perpendicular to the radial direction would limit fission product release.

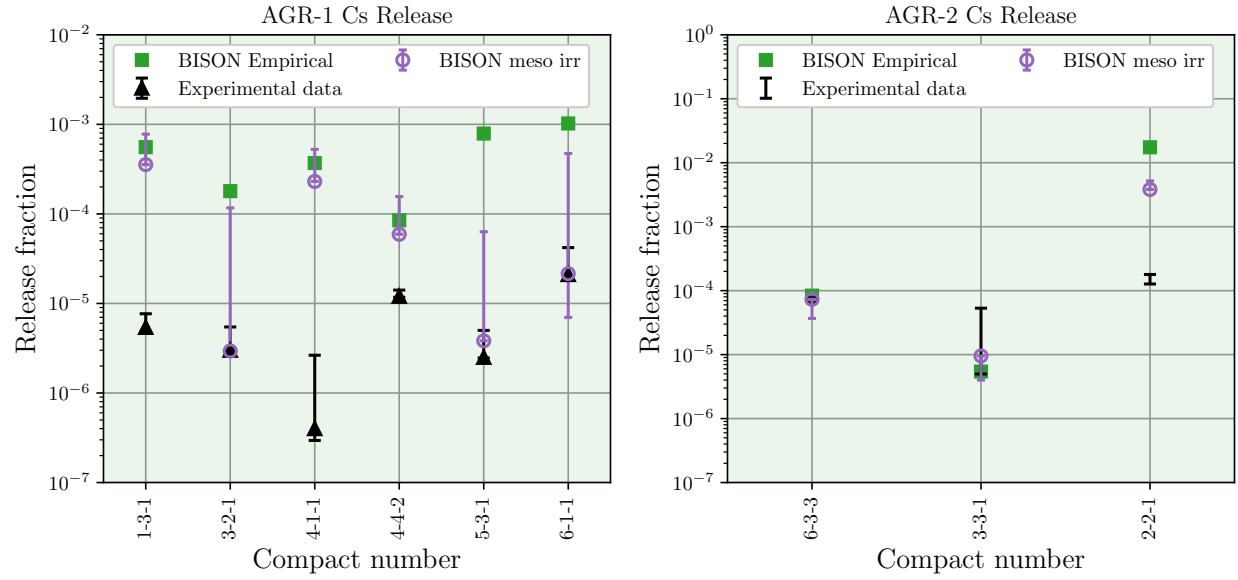


Figure 5.1. Comparison of measured (post-irradiation examination (PIE)) and computed (BISON) Cs release fractions for AGR-1 compacts. The BISON results show the values obtained with the empirical BISON diffusivity from Christ [21] (green), as well as the results obtained by the current study with the new mesoscale effective Cs diffusion coefficient defined in Eqs. (4.4) to (4.7) with coefficients from Table 4.2 (purple). The ranges shown for the mesoscale diffusion coefficient correspond to the minimum and maximum grain minor axis size for each as-fabricated compact provided in Ref. [33], and the markers correspond to the optimized values (as listed in Table 5.1). Using $D_{corr}^{eff, tot}$ improves the predicted Cs release fraction in all cases.

6. PALLADIUM ATTACK OF SiC

6.1 Description of the Pd attack of SiC

At high temperatures, Pd reacts with SiC to form various palladium silicides (PdSi, Pd₂Si, Pd₃Si, Pd₅Si₂, Pd₅Si). At lower temperatures, this reaction proceeds via a solid state mechanism



where x is the average stoichiometry of the palladium silicide layer. This stoichiometry varies with temperature, increasingly approaching 2.0 as the temperature increases above 1000°C [41]. The presence of Pd in the SiC is thought to enhance Ag release through the formation of Pd-Ag-Si solution [42]. Ag lowers the melting point of Pd, allowing the reaction to proceed faster via the liquid state mechanism at lower temperatures [43, 44]. The Ag has a higher solubility in the liquid phase than in the SiC, which can potentially enhance the Ag release rate [42]. The work in this section is limited to the solid state reaction, but the effect of a liquid phase will be explored in the future.

In solid state reactions of Pd with SiC, the formation of periodic layered lamellae consisting of silicide-rich and carbon-rich regions is observed. The mechanisms governing the formation of these layered lamellae are not well understood [45]. It has been suggested that the layered structures form as a result of the slow diffusion of C, causing the graphitic carbon formed during the reaction to get stuck at the reaction front, resulting in the formation of a new Kirkendall plane [46]. The Pd continues to diffuse through the newly formed C layer and reacts with SiC at the graphite/SiC interface, resulting in the formation of a new Pd _{x} Si layer. This process then repeats itself, resulting in a periodic layered microstructure consisting of C and Pd rich layers [44]. In this section, a phase-field model is developed to test this hypothesis.

6.2 Model development

6.2.1 Grand-potential-based model

The phase-field model has been widely used in literature to model the evolution in processes such as solidification, grain growth, and phase separation [47, 48, 49]. Microstructural features such as grains and phases are represented using non-conserved order parameter (OP) variables. Component atomic fractions are represented using conserved variable fields.

In this work, a grand-potential-based phase-field model was developed for the Pd-Si-C system. In grand-potential formulation, the chemical potentials are treated as the independent variables rather than the component atomic fractions. This allows the grand-potential-based phase-field model to control the interface thickness independently of the interface energy [50, 51].

Three phases are considered in the model: graphite, Pd₂Si, and SiC. The other palladium silicide phases are not modeled in this work to simplify model development. Pd₂Si was chosen as the representative palladium silicide phase because it has the lowest Gibbs energy of formation among the palladium silicide phases. The Pd and C chemical potentials are treated as the independent variables in this formulation. The diffusion is then modeled by solving

$$\chi_i \frac{d\mu_i}{dt} = \nabla D_i \chi_i \nabla \mu_i - \sum_j \frac{d\rho_i}{d\eta_j} \frac{d\eta_j}{dt}, \quad (6.2)$$

where μ_i is the chemical potential of component i , χ_i is the susceptibility, D_i is the diffusivity, ρ_i is the concentration, and η_j is the OP. The concentration of the component can be calculated from

$$\rho_i = \frac{c_i}{V_a}, \quad (6.3)$$

where V_a is the atomic volume, and c_i is the atomic fraction.

The OPs are evolved by solving the Allen-Cahn equation

$$\frac{d\eta_j}{dt} = -L \frac{d\Omega}{d\eta}, \quad (6.4)$$

where Ω is the grand-potential of the system. The grand-potential is computed by applying a Legendre transform to the Helmholtz free energy. The grand-potential of the system is calculated as

$$\Omega = \int_V (\omega_{chem} + \omega_{int}) dV, \quad (6.5)$$

where ω_{chem} and ω_{int} are the chemical and interfacial grand-potential density contributions. The interfacial grand-potential density contribution is calculated using

$$\omega_{int} = m f_0 + \sum_j \frac{\kappa}{2} |\nabla \eta_j|^2 \quad (6.6)$$

$$f_0 = \left(\frac{\eta_j^4}{4} - \frac{\eta_j^2}{2} \right) + \sum_{k=1}^p \sum_{\alpha=1}^p \frac{\gamma}{2} \eta_k^2 \eta_\alpha^2 + \frac{1}{4}, \quad (6.7)$$

where m is the barrier height, κ is the gradient energy coefficient, p is the number of OPs in the system, f_0 is the barrier energy function, and $\gamma = 1.5$ is used so that the OP profiles through the interface are symmetric [52]. The barrier height and gradient energy coefficients can be computed as functions of the interface energy σ and interface width l

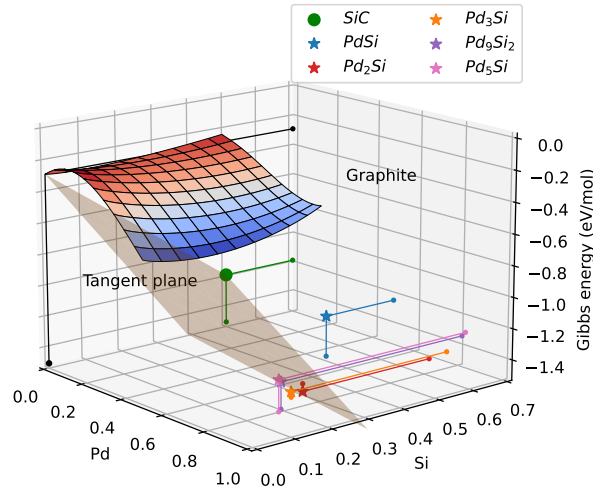


Figure 6.1. Free energy of Pd-Si-C system as a function of the composition at $T = 1200$ K. Graphite is the only substitutional phase and has a non-convex free energy function. All other phases are stoichiometric compounds.

using

$$m = \frac{6\sigma}{l}, \quad (6.8)$$

$$\kappa = \frac{3\sigma l}{4}, \quad (6.9)$$

allowing us to freely change the interface width of the phase-field model without changing the interface energy [52]. The chemical grand-potential density is interpolated between phases

$$\omega_{chem} = \sum_j h_j \omega_j, \quad (6.10)$$

where h_j is a switching function that is used to interpolate between the three phases. The model uses a multi-phase switching function that has the form [53, 51]

$$h_j = \frac{\eta_j^2}{\sum_k \eta_k^2}. \quad (6.11)$$

Fig. 6.1 shows the CALPHAD assessment free energies of SiC, graphite, and the palladium silicides as a function of the Pd and Si content [54, 55]. The original CALPHAD free energy is non-convex and has log-terms. The grand-potential model requires analytical inverses for the chemical potential expressions and cannot be used directly with this complex free energy function.

Instead, a Python script is used to derive the equilibrium composition of the system. A polynomial free energy expression is then fitted for each phase to the CALPHAD free energy at the equilibrium point, as a function of the

Table 6.1. Material property values for Pd-Si-C system, including the description, variable, value, and the reference where the value was obtained.

Description	Variable	Value	Reference
Temperature	T	1200 K	
Atomic volumes	V_a	$0.0207417366 \text{ nm}^3 \text{ atom}^{-1}$	[56]
Interface energy	σ_S	5 J/m^2	[57]
Polynomial free energy parameters	G_0	-1.658582 eV/atom	
	A_{Pd}	0.5069414 eV/atom	
	$c_{Pd,eq}^{Gr}$	$1.04612598\text{e-}12$	
	$c_{Pd,eq}^{SiC}$	0.0	
	$c_{Pd_2Si,eq}^{Pd,eq}$	0.67	
	A_C	0.5069414 eV/atom	
	$c_{C,eq}^{Gr}$	$9.99999892\text{e-}01$	
	$c_{C,eq}^{SiC}$	0.5	
	$c_{C,eq}^{Pd_2Si}$	0.0	
	B_{Pd}	$2 \times 10^4 \text{ eV/atom}$	
	B_C	$2 \times 10^4 \text{ eV/atom}$	
Diffusion coefficient	D_{Pd}	$142.53 \text{ nm}^2 \text{ s}^{-1}$	[58]
Allen-Cahn mobility	L	$8 \times 10^{-5} \text{ nm}^3 \text{ eV}^{-1} \text{ s}^{-1}$	

phase concentrations of Pd and C. This free energy takes the form

$$f_\beta = G_0 + \sum_i \left(A_i c_i^\beta + \frac{1}{2} B_i (c_i^\beta - c_{i,eq}^\beta)^2 \right), \quad (6.12)$$

where G_0 , A_i , and B_i are the polynomial fit parameters, and $c_{i,eq}^\beta$ is the multi-phase equilibrium mole fraction of the component i in phase β . The values of the polynomial fit parameters are calculated such that the free energy and its first and second-order derivatives with respect to the mole fractions match between the CALPHAD and polynomial free energies at the multi-phase equilibrium composition. Table 6.1 shows the calculated values of the polynomial free energy parameters. The calculated values of $B_{Pd} = 9.89 \times 10^{10}$ and $B_C = 9.56 \times 10^6$ are too large and result in poor model convergence. A value of 10^4 for both parameters was found to be adequate to get good convergence and prevent negative atomic fractions in the simulation.

The chemical potential is defined as the first derivative of the free energy with respect to the phase mole fraction

$$\mu_i^\beta = A_i + B_i (c_i^\beta - c_{i,eq}^\beta). \quad (6.13)$$

In the grand-potential formulation, phase mole fractions are calculated by inverting the expression for the chemical potential

$$c_i^\beta = \frac{(\mu_i^\beta - A_i)}{B_i} + c_{i,eq}^\beta. \quad (6.14)$$

The susceptibility can then be calculated using the derivative of the phase mole fraction with respect to the chemical potential

$$\chi_i^\beta = \frac{1}{B_i}. \quad (6.15)$$

The chemical grand-potential density is derived by taking the Legendre transform of Eq. 6.12

$$\omega_\beta = \frac{1}{V_a} \left(G_0 - (\mu_C - A_C)^2 / B_C - (\mu_C - A_C) c_{C,eq}^\beta \right. \quad (6.16)$$

$$\left. - (\mu_{Pd} - A_{Pd})^2 / B_{Pd} - (\mu_{Pd} - A_{Pd}) c_{Pd,eq}^\beta \right). \quad (6.17)$$

The value of the diffusion coefficient of Pd in graphite was used in all phases, due to the difficulty of obtaining values for Pd diffusivity in the stoichiometric phases. For carbon, the diffusion coefficient was calculated as

$$D_C = D_{Pd} \left(h_{Pd_2Si} + R(h_{SiC} + h_{Gr}) \right), \quad (6.18)$$

where R is the ratio of diffusivity of C and Pd. The value of R is varied to study the impact of carbon diffusivity on the silicide microstructure evolution.

The Pd attack of SiC was simulated using a 2D simulation domain. Figure 6.2a shows the initial condition of the system. The system models a domain of $550 \text{ nm} \times 40 \text{ nm}$. From left to right, 25 nm of graphite, 25 nm of Pd_2Si , and 500 nm of SiC phases are initialized. The initial amount of SiC in the system was kept large enough that the system evolution is not limited by the availability of SiC for the Pd to react with. A small amount of graphite and Pd_2Si are initialized as initial seeds for phase growth. The chemical potentials of Pd and C are set so that the system is at equilibrium. A Neumann boundary condition is placed on μ_{Pd} to drive a constant flux of Pd into the system. In the results in Fig. 6.2, the flux is set to $2.074 \times 10^{-6} \text{ atoms s}^{-1} \text{ nm}^{-2}$. This value results in a 50 nm increase in the average thickness of the Pd_2Si layer over the 10^6 s of simulation. We then run the simulation with five values of ratio of diffusivity of C and Pd - $R = 10^0, 10^{-1}, 10^{-2}, 10^{-3}, \text{ and } 10^{-4}$.

To study the effect of the flux of Pd on the microstructure evolution, two 2D simulations were run. In both simulations, $R = 10^{-3}$. The first simulation is run with a flux of $2.074 \times 10^{-6} \text{ atoms s}^{-1} \text{ nm}^{-2}$ for 10^5 s . The second simulation is run with a flux of $2.074 \times 10^{-7} \text{ atoms s}^{-1} \text{ nm}^{-2}$ for 10^6 s . The initial condition of the simulations is shown in Fig. 6.3a. The microstructures formed after the high and low flux simulations are shown in Figs. 6.3b and 6.3c, respectively. In the high flux simulation, new graphite and Pd_2Si phases are formed, while in the low flux simulation, only the initial grains are observed to grow. The total increase in graphite and Pd_2Si phases is the same in both cases.

6.2.2 Numerical methods development

As discussed in Section 6.2.1, the grand-potential model cannot be used with free energy expressions that do not have an analytical solution to the equipotential condition. Additionally, the grand-potential model is prone to mass conservation

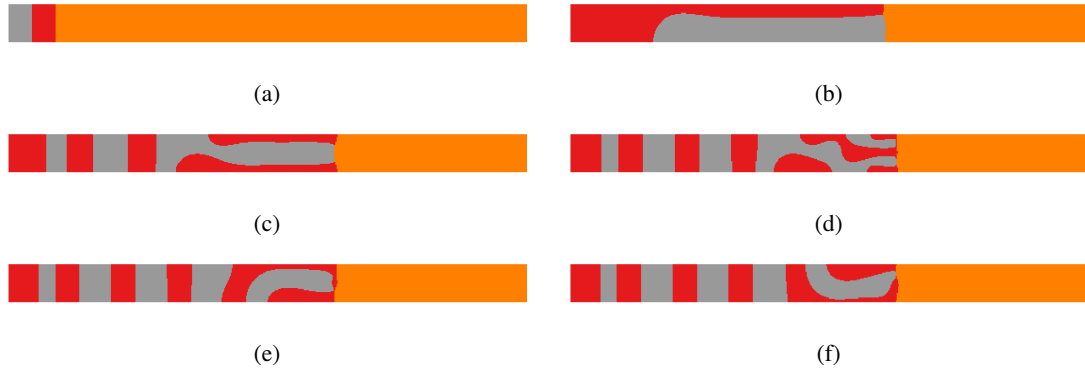


Figure 6.2. Effect of D_C/D_{Pd} on microstructure formed during Pd attack of SiC. The graphite, Pd_2Si and SiC phases are represented by grey, red, and orange colors, respectively. (a) shows the initial condition of the system. (b), (c), (d), (e), and (f) show the microstructure formed after 10^6 s with the ratio of D_C/D_{Pd} set to 10^0 , 10^{-1} , 10^{-2} , 10^{-3} , and 10^{-4} , respectively. As the carbon diffusivity becomes smaller, the graphite and Pd_2Si start growing in bands perpendicular to the direction of Pd flux.

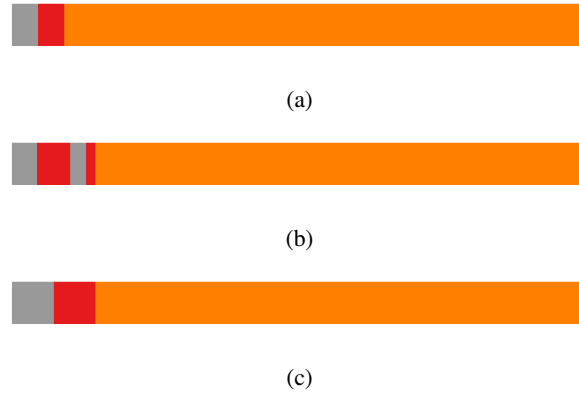


Figure 6.3. Effect of Pd flux J_{Pd} on microstructure formed during Pd attack of SiC. The graphite, Pd_2Si , and SiC phases are represented by grey, red, and orange colors, respectively. (a) shows the initial condition of the system. (b) and (c) show the microstructure formed after 10^5 s with $J_{Pd} = 2.074 \times 10^{-6} \text{ atoms s}^{-1} \text{ nm}^{-2}$ and 10^6 s with $J_{Pd} = 2.074 \times 10^{-7} \text{ s}^{-1} \text{ nm}^{-2}$, respectively. In both cases, the total amount of Pd entering the system is same, and the total increase in Pd_2Si and graphite phases is the the same. The lower Pd flux results in growth of the pre-existing phases, whereas the higher flux in (b) causes the nucleation and growth of new Pd_2Si and graphite regions.

errors [59]. The Kim-Kim-Suzuki (KKS) method numerically solves the equipotential condition

$$\frac{df_1}{dc_i^1} = \frac{df_2}{dc_i^2} = \dots = \mu_i. \quad (6.19)$$

This allows using more complex free energy functions for phase-field models than the grand-potential approach. It also does not suffer from the mass conservation issues of the grand-potential model. However, the current KKS implemen-

tation in MOOSE has several limitations.

First, KKS uses non-linear variables for every phase concentration. The number of phase concentration variables is equal to the $p \times n$, where n is the number of components, and p is the number of phases. Compared to this, the grand-potential model uses material properties for all the phase concentrations. As a result, the cost of running KKS simulations increases rapidly as the number of components and phases in the system increases.

Second, when the free energy expression has log terms, the equipotential condition has discontinuities where the concentration of any component becomes zero. This makes the equipotential condition very difficult to solve with the standard Newton method when the solutions are close to zero. Additionally, if the initial guess is far from the solution, the nonlinear iteration can create a guess that is outside the stability region of Newton method. This can again cause the guess to fall outside the trust region, and the Newton method will fail to converge. As a result, although in theory KKS can be used for any convex free energy expression, in practice, simplified free energies are required to get reasonable convergence out of the models. This prevents using CALPHAD free energies from being used in phase-field model development.

The graphite free energy has log terms, and the Pd atomic fraction in graphite at equilibrium is between 10^{-10} – 10^{-15} based on the system temperature. The KKS model does not converge at these low atomic fractions, and polynomial approximations of the free energy do not capture the highly non-linear curvature of the log terms. Polynomial approximations can therefore result in unphysical behavior, such as negative atomic fractions, and incorrect predictions of driving forces when the system is far from equilibrium. This limits the accuracy of model predictions.

To work around this problem, a nested damped Newton method is being developed in MOOSE. The nested Newton approach implements a second Newton method loop inside a material property. The equipotential condition is then solved to calculate phase concentrations as material properties. The phase concentrations are then used to calculate the driving forces for component diffusion and phase evolution using new nested Newton kernels.

The nested Newton approach still does not fix the convergence issues for free energies with log terms. In problems with trust regions for the function to be minimized, the non-linear iterations can be damped to reduce the step size until certain conditions are met. In the equipotential condition with log terms, this condition is

$$\forall i \forall j c_i^j > 0, \quad (6.20)$$

where i is the component, and j is the phase. This includes the dependent phase concentrations in substitutional lattices. The damped nested Newton algorithm scales down the nonlinear iteration step size by a user-inputted factor α until this condition is satisfied. This ensures that the nonlinear iteration guess never falls outside the trust region, allowing the Newton method to converge log free energies.

As a demonstration problem, the corrosion of Ni-Cr alloys in molten FLiBe was simulated using the damped nested Newton KKS model. The model has two components, Ni and Cr, and two phases, metal and molten salt. Both phases have log-based free energy expressions and have been previously detailed in a publication [60]. The dependent component atomic fraction is very small in the metal phase ($\approx 2 \times 10^{-7}$), and the Ni atomic fraction is very small in the molten-salt phase (8×10^{-9}). This makes it very difficult to simulate the system using the standard KKS model. Using the damped nested Newton method developed in this work, we can now simulate the corrosion process as shown in Fig. 6.4. This approach will be expanded and applied to the Pd-C-SiC system to improve model accuracy and

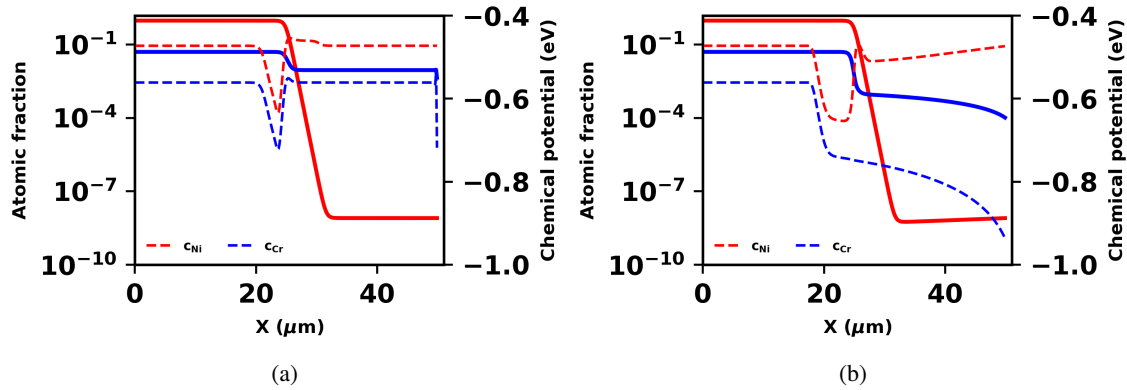


Figure 6.4. Simulating Ni-Cr corrosion in molten FLiBe salt. The solid lines show the atomic fraction of the Ni and Cr, and the dotted lines show the chemical potential calculated by solving the equipotential condition. (a) shows the initial condition of the system; (b) shows the chemical potential evolution after 10^4 s.

computational cost.

6.3 Discussion

As seen in Fig. 6.2, as the ratio of diffusivity of C and Pd, R , becomes smaller, the microstructure of the Pd_2Si and graphite phases changes from a columnar structure growing in the direction of the Pd flux to a lamellar structure. As the simulation progresses, the lamellar structure breaks down, and a more columnar growth starts again. As R decreases, the number of lamellar layers that form before the columnar growth increases. In Figs. 6.2d to 6.2f, we observe that the graphite layer thickness in the lamellae is twice that of the Pd_2Si layers, and the layer thickness remains constant until the structure breaks down. As the reaction proceeds, the Pd_2Si layers move toward the Pd source, and the graphite moves in the opposite direction.

In Fig. 6.3 the total increase in the Pd_2Si and graphite phase volumes is equal in both the high and low flux cases. This is expected as the total amount of Pd entering the system is the same. However, the high flux simulation demonstrates the formation of a new lamellar layer, while in the low flux case only the pre-existing Pd_2Si and graphite phases grow. In the lower flux case, there is plenty of time for C to diffuse through the Pd_2Si layer. In the high flux case, the growth of the pre-existing phases is limited by diffusion of C, and new phases nucleate due to the system crossing into the spinodal decomposition region of the free energy. Both results from Sec. 6.2.1 support the hypothesis that the difference in mobility between carbon and palladium results in the formation of the lamellar microstructure.

The layers of the lamellae observed in the simulations are on a length scale of 10s of nanometers, whereas in experimental data these layers have been observed to have length scales of $20\text{ }\mu\text{m}$ [44]. This suggests that while the current model captures the fundamental mechanism driving the formation of the observed microstructure, better parameterization of the model is required to accurately capture the length scale of the microstructure.

Additionally, the lamellar structure in the 2D simulations breaks down after a only a few layers. It is not yet fully understood what causes this behavior. One possibility is that this is caused by boundary effects resulting from the small

size of the simulation domain in the direction perpendicular to the Pd flux.

The damped nested Newton method being implemented in MOOSE will allow the simulation of the complex multi-component free energies that is required to fully understand the microstructure evolution of SiC under Pd attack. This new approach combines the lower memory requirements and fast convergence of the grand potential approach with the flexibility in choosing free energy expressions and mass conservation of the KKS approach.

In the future, this model will be parameterized using more accurate material properties from literature or lower length scale modeling. Larger domain size simulations are needed to understand the impact of boundary conditions and SiC grain structure on the silicide growth. The numerical methods development described in Section 6.2.2 will be used to capture the system thermodynamics more accurately without relying on polynomial approximations.

The model will be expanded to account for the impact of Ag on the Pd attack. This will include adding the melt phase and the effect of Ag on the model thermodynamics and kinetics. The model will then be used to calculate the effective transport rate of Ag and Pd. The effect of a concentrated Pd source on the microstructure evolution and mass transport will be studied to understand Ag and Pd release in a TRISO particle with a cracked IPyC layer. These results will inform the BISON Pd penetration failure model and Ag release model.

7. IMPROVEMENT OF THE MODEL FOR Ag DIFFUSION IN SiC

7.1 New estimate of Ag diffusion in SiC in different GB types using a new potential for MD calculations

In Section 3, we have obtained new predictions of Ag diffusivities in SiC GBs using a newly developed empirical potential. These values will be employed in this section to further improve the model for Ag diffusion in SiC. As shown in Figure 7.1, MD simulations with the old potential [61], which was employed in our previous study [3], lead to significantly higher activation energy for Ag diffusion in $\Sigma 5$ GB. The impact of the updated GB diffusivity on effective diffusivity, as well as the impact of the presence of different types of GBs and the percolation of LAGBs, is considered in this section.

7.2 Impact on mesoscale effective Ag diffusivity in SiC

Ag release has been observed to occur from TRISO particles with an intact SiC layer [2]. Due to the long half-life of the Ag (^{110m}Ag) isotope, Ag release is an important safety concern. In polycrystalline microstructures, Ag release can be assisted by the GB network [3, 4, 5]. In GB networks, LAGBs were determined to promote faster Ag diffusion than HAGBs [5], with a potentially significant effect on the effective mesoscale diffusivity. Therefore, we studied the influence of GB type distribution in the SiC microstructure on effective Ag diffusivity in polycrystalline SiC.

In this section, we start by determining the effective diffusivity of Ag in SiC assuming that the GBs are either all HAGBs or all LAGBs. This will provide a range of diffusivity values for realistic microstructures with a mix of LAGBs and HAGBs. Note that since two different sets of HAGB and LAGB diffusivities have been derived (one for the existing potential, one for the newly developed potential—see Chapter 3 and Section 7.1), we perform these simulations for both and compare their performance. Once the effective diffusivity for the all LAGBs or all HAGBs microstructure are completed, we determine the effective diffusivity in microstructures with mixed GB types and propose metrics to quantify the texture and link it to effective diffusivity.

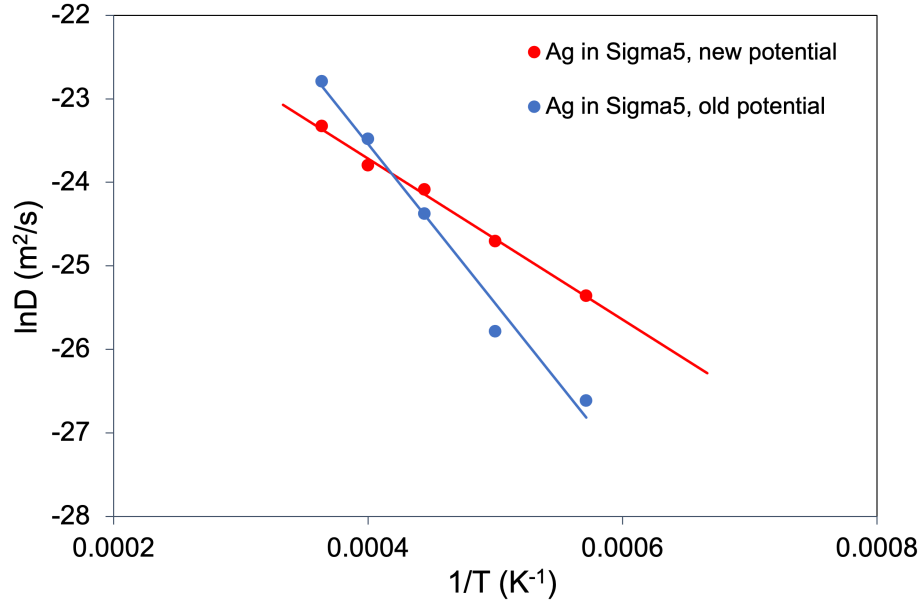


Figure 7.1. Arrhenius plot for Cs and Ag diffusivities within the $\Sigma 5$ (210)/[001] GB of SiC. The solid lines represent the best fitting of MD data using the Arrhenius equation.

7.2.1 Method for effective Ag diffusivity

As described in Section 4.2, we used the AEH approach in MOOSE to calculate the effective diffusivity in microstructures obtained in Ref. [3, 4]. The flux used in simulations includes 0, 4.7×10^{13} n/m²/s and every order of magnitude up to 4.7×10^{18} n/m²/s. The temperature in the simulations varies from 1000 K to 2000 K with intervals of 200 K.

7.2.2 Effective Ag diffusivity calculation in fully LAGB and fully HAGB microstructure

Using the diffusivities for LAGB, HAGB, and grain bulk calculated using atomistic scale techniques in Refs. [3, 5] and Section 7.1 with the newly developed potential, we determined effective Ag diffusivity at different temperatures and fluxes in SiC microstructures assuming that the GBs were either all HAGBs or all LAGBs. The effective diffusivity results are shown in Fig. 7.2 with solid points. The grey points are the results of microstructures exclusively with LAGBs, and the brown points are from the results of microstructures with HAGBs. These results were fitted using the approach detailed in [5]. The coefficients for thermal Ag diffusion with the fully HAGB microstructures are $D_{m,0} = 2.19 \times 10^{-13}$ m²/s, $D_{m,1} = -1.59 \times 10^{-7}$ m/s, $Q_{m,0} = 8.19 \times 10^4$ J/mol, and $Q_{m,1} = 4.25 \times 10^9$ J/mol/m. The quality of the fit for the pre-exponential factor and the energy barrier are equal to $R^2 = 0.955$ and $R^2 = 0.986$, respectively. The coefficients c_i^{irr} with the fully HAGB microstructures are $c_0^{irr} = 9.99 \times 10^{-14}$ (n/m²/s)⁻¹, $c_1^{irr} = 0.656$ (-), $c_2^{irr} = 3.60 \times 10^6$ m⁻¹, and $c_3^{irr} = -3.50 \times 10^4$ J/mol. The coefficients for thermal Ag diffusion with the fully LAGB microstructures are $D_{m,0} = 2.73 \times 10^{-12}$ m²/s, $D_{m,1} = -2.32 \times 10^{-6}$ m/s, $Q_{m,0} = 7.02 \times 10^4$ J/mol, and $Q_{m,1} = 1.94 \times 10^8$ J/mol/m. The quality of the fit for the pre-exponential factor and the energy barrier are equal to $R^2 = 0.956$ and

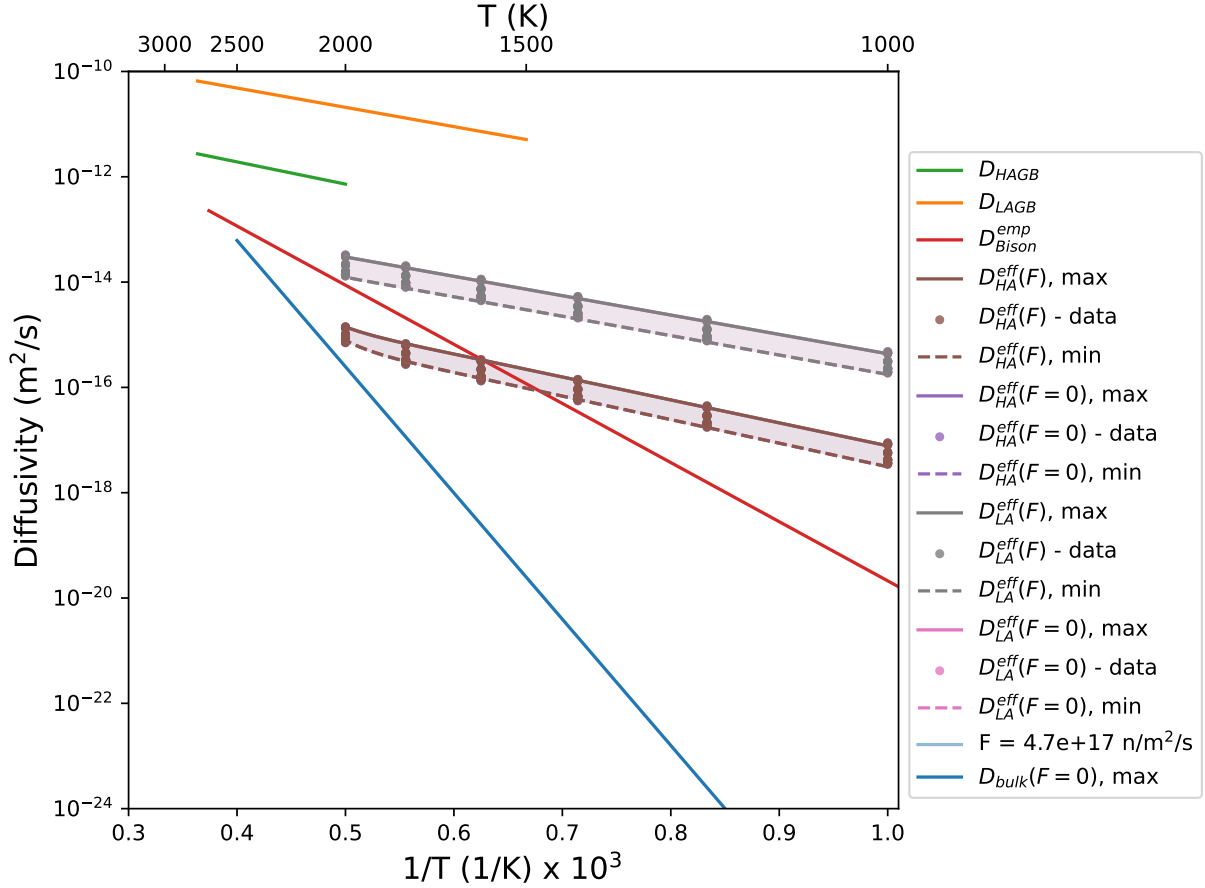


Figure 7.2. Comparison of the Ag diffusion coefficients provided by atomistic simulations (bulk diffusivity, HAGB diffusivity, and LAGB diffusivity), the empirical coefficient D_{emp}^{BISON} previously used in BISON [14, 62, 1, 63], and the effective Ag diffusivity values provided by the current mesoscale study $D^{eff,tot}$ for Ag—Eqs. (4.4) to (4.6). The different values for $D^{eff,tot}$ at each temperature correspond to the extreme grain minor axis length values of the SiC microstructures described in Section 4.1 (solid line for smallest minor axis size, dashed lines for largest minor axis size) and different flux values ($D^{eff,tot}$ for 0 flux, $D^{eff,tot}(F)$ for flux = 4.7×10^{17} n/m²/s).

$R^2 = 0.927$, respectively. The coefficients c_i^{irr} with the fully LAGB microstructure are $c_0^{irr} = 8.80 \times 10^{-15}$ (n/m²/s)⁻¹, $c_1^{irr} = 0.673$ (-), $c_2^{irr} = 4.20 \times 10^6$ m⁻¹, and $c_3^{irr} = -5.90 \times 10^4$ J/mol. The grey and brown curves are from the fitting equation. The solid curves at the upper limit of these points are from the smallest minor axis size, and the dashed curves at lower limit are from the largest minor axis size. The upper and lower limit from the fitting equation bound all the simulation results. The minor difference between zero flux and 4.7×10^{17} n/m²/s of flux shows the low influence of flux on effective diffusivity, which is attributed to the fact that GB diffusivity dominates at low temperatures where irradiation-enhanced bulk diffusivity is expected.

We also used old GB diffusivity data with higher activation energy on the fully LAGB and fully HAGB microstruc-

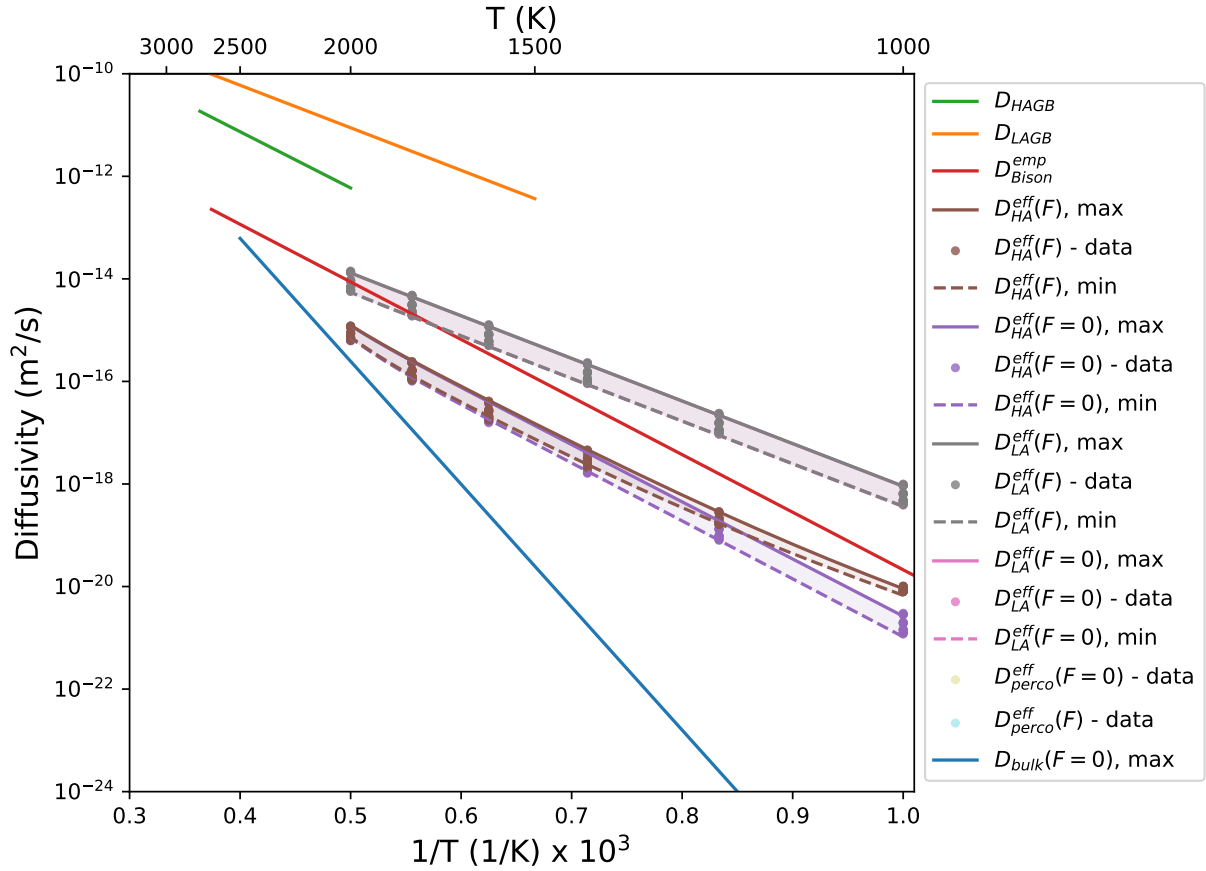


Figure 7.3. Comparison of the Ag diffusion coefficients provided by old atomistic simulations with GB diffusivity of higher activation energy (bulk diffusivity, HAGB diffusivity, and LAGB diffusivity) [3], the empirical coefficient D_{emp}^{BISON} previously used in BISON [14, 62, 1, 63], and the effective Ag diffusivity values provided by the current mesoscale study $D^{eff, total}$ for Ag—Eqs. (4.4) to (4.6). The different values for $D^{eff, tot}$ at each temperature correspond to the extreme grain minor axis length values of the SiC microstructures described in Section 4.1 (solid line for smallest minor axis size, dashed lines for largest minor axis size), and different flux values ($D^{eff, tot}$ for 0 flux, $D^{eff, tot}(F)$ for flux = 4.7×10^{17} n/m²/s).

tures [3]. The effective diffusivities from AEH simulations are presented in Fig. 7.3. The updated coefficients for thermal Ag diffusion for fully HAGB microstructures are $D_{m,0} = 4.55 \times 10^{-10}$ m²/s, $D_{m,1} = -3.08 \times 10^{-4}$ m/s, $Q_{m,0} = 2.12 \times 10^5$ J/mol, and $Q_{m,1} = 5.44 \times 10^9$ J/mol/m. The quality of the fit for the pre-exponential factor and the energy barrier are equal to $R^2 = 0.953$ and $R^2 = 0.987$, respectively. The coefficients c_i^{irr} for fully HAGB microstructures are $c_0^{irr} = 4.41 \times 10^{-13}$ (n/m²/s)⁻¹, $c_1^{irr} = 0.459$ (-), $c_2^{irr} = 8.11 \times 10^6$ m⁻¹, and $c_3^{irr} = 7.84 \times 10^4$ J/mol. The updated coefficients for thermal Ag diffusion for fully LAGB microstructures are $D_{m,0} = 2.43 \times 10^{-10}$ m²/s, $D_{m,1} = -2.04 \times 10^{-4}$ m/s, $Q_{m,0} = 1.59 \times 10^5$ J/mol, and $Q_{m,1} = 4.74 \times 10^8$ J/mol/m. The quality of the fit for the

pre-exponential factor and the energy barrier are equal to $R^2 = 0.956$ and $R^2 = 0.941$, respectively. The coefficients c_i^{irr} for fully LAGB microstructures are $c_0^{irr} = 1.84 \times 10^{-13} \text{ (n/m}^2\text{/s)}^{-1}$, $c_1^{irr} = 0.499 \text{ (-)}$, $c_2^{irr} = 4.46 \times 10^6 \text{ m}^{-1}$, and $c_3^{irr} = 2.80 \times 10^4 \text{ J/mol}$. Since GB diffusivity is lower with the older potential, the irradiation effects now make the $D_{HA}^{eff}(F)$ apparently larger than $D_{HA}^{eff}(F = 0)$ in fully HAGB microstructures at lower temperatures. The empirical diffusivity from BISON falls within the range between D_{HA}^{eff} and D_{LA}^{eff} when the potential from Ref. [61] is used.

As shown in Figs. 7.2 and 7.3, the different sets of LAGB and HAGB diffusivities provided by the two different potentials lead to significantly different effective diffusivities. This observation warrants future investigation of GB diffusivities to reduce the associated uncertainty, including consideration of different types of LAGBs. In the meantime, the mesoscale results obtained with the potential from Ref. [61] better match experimental observations.

7.2.3 Description of SiC microstructure for Ag diffusion

To study the effect of texture and GB type distribution, we used the 20 2D polycrystalline domains of dimensions $9 \mu\text{m} \times 9 \mu\text{m}$, the same microstructures as used in Section 4.1. For each microstructure, we generated four different GB type distributions with mixtures of HAGBs and LAGBs; examples of which are shown in Fig. 7.4. The yellow GBs are HAGBs, and the green GBs are LAGBs. Each case in Fig. 7.4 has a different LAGB fraction. We also considered microstructures that were fully LAGB and fully HAGB. These microstructures were obtained using the approach described in [3, 4, 5, 31]. Starting from an artificially generated grain orientation distribution with the

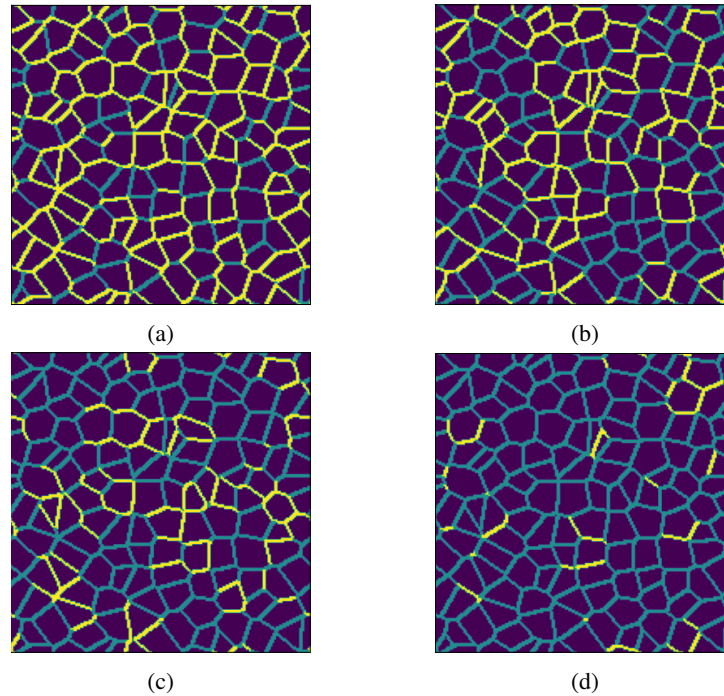


Figure 7.4. Examples of microstructures with mixed GB types with different LAGB fractions. The yellow GBs are HAGBs, and the green GBs are LAGBs. The LAGB fractions are (a) 0.3, (b) 0.5, (c) 0.7, and (d) 0.9.

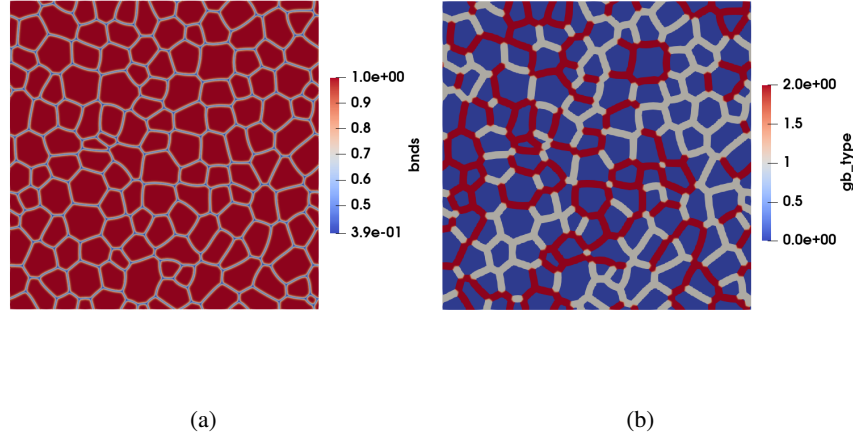


Figure 7.5. One smoothed microstructure after grain growth. (a) is the smoothed microstructure; (b) is the microstructure with distinguished GB type. In (b), grain interiors are shown in blue, LAGBs are shown in grey, and HAGBs are shown in red.

derived grain size and shape with a set grain aspect ratio, a grain growth model was run in MOOSE for 10,000s^a to obtain a microstructure with the desired GB width. The width of the GBs for all the microstructures is scaled up to 60 nm using the method derived in [3, 4] to minimize computational costs. During the grain growth simulation, we determine the GB type with the “ComputeGBMisorientationType” feature in MOOSE [5]. LAGBs correspond to a misorientation angle lower than 15°; HAGBs correspond to a misorientation angle higher than 15°. One example of the resulting continuous microstructures with distinguished GB type is shown in Fig. 7.5.

7.2.4 Percolation parameters from the microstructure

Due to the higher diffusivity of LAGBs relative to HAGBs as calculated for Ag in SiC, the effective diffusivity can be dominated by the distribution of LAGB in the polycrystal. This depends, however, on the polycrystalline texture and whether the distribution of LAGBs provides a diffusion pathway. In this work, we explore different ways of defining a percolation parameter P to quantify the distribution of LAGBs. The goal is to identify a percolation definition that correlates to calculated effective diffusivity. This would enable the development of a texture-dependent effective diffusivity.

The different metrics to characterize percolation considered in this study are (1) the number fraction of LAGBs over all GBs [64, 65], (2) the area fraction of LAGBs over all GBs, (3) the area fraction of the largest LAGB cluster or LAGB cluster strength, and (4) the weighted average length of the LAGB clusters along the diffusion direction. Frary and Schuh [66] also provide several potential parameters to describe the scaling law in percolation.

^aExcept one simulation which was run for 9,300 s due to numerical instability. The final microstructure, however, had the desired GB width and was ready to be used.

The number fraction of LAGB, f_{num} , is given by

$$f_{num} = \frac{n_{LAGB}}{n_{GB}}, \quad (7.1)$$

where n_{LAGB} and n_{GB} are the number of LAGB and GB in the microstructure, respectively. Because microstructures can have different grain aspect ratios, the area fraction of LAGB can represent the distribution of LAGB more accurately than the number fraction of LAGB. The area fraction of LAGB, f_{area} , is defined as

$$f_{area} = \frac{\sum_i^{LAGB} A_i}{\sum_i^{GB} A_i}, \quad (7.2)$$

where i is the index of each GB, and A_i is the area of the corresponding GB. The LAGB cluster strength, $s_{cluster}$, is the area fraction of the largest (in terms of area) LAGB cluster over the area of all GBs. A LAGB cluster is defined as a continuously connected network of LAGBs. The LAGB cluster strength is defined as

$$s_{cluster} = \frac{\max_{j=LAGB} A_j}{\sum_j^{GB} A_j}, \quad (7.3)$$

where j is the index of each GB cluster in the microstructure, and A_j is the area of the GB cluster with index j . Because $s_{cluster}$ only characterizes the influence of the maximum size cluster, it might underestimate percolation. We therefore also characterize percolation by the weighted average length of LAGB cluster, $L_{cluster}$, which is defined as

$$L_{cluster} = \frac{\sum_j^{LAGB} A_j l_j}{D}, \quad (7.4)$$

where l_j is the length of the cluster with index j in diffusion direction, and d is the length of the domain in the diffusion direction. All these percolation parameters vary from 0 to 1.

We used the existing ‘‘Grain Tracker’’ feature in MOOSE to discern the unique GB index and GB cluster index [34].^b One example with unique LAGBs index and LAGB clusters index is shown in Fig. 7.6. The feature can also output the area and central coordinate for each GB or cluster to calculate the four percolation parameters. These four percolation parameters will be used to characterize the GB type distribution (i.e., the LAGB percolation). We expect different performances from the different definitions and will evaluate the one that best correlates to and therefore predicts effective diffusivity. In the following section, we compared their performance.

7.2.5 Effective Ag diffusivity calculation in microstructure with percolation

In Figs. 7.2 and 7.3, the difference between D_{HA}^{eff} and D_{LA}^{eff} varies from four orders of magnitude to one order of magnitude from 1000 K to 2000 K. The effective diffusivity results from microstructures with different GB type distributions are also presented as $D_{perco}^{eff}(F = 0)$ and $D_{perco}^{eff}(F)$ in Fig. 7.7. The large difference suggests the importance of percolation of high-diffusivity GBs to accurately predict the effective diffusivity. Therefore, we tested the percolation

^bNote that the ‘‘Grain Tracker’’ feature cannot find the GBs with trivial length, which decreases the accuracy of fraction by number of LAGB.

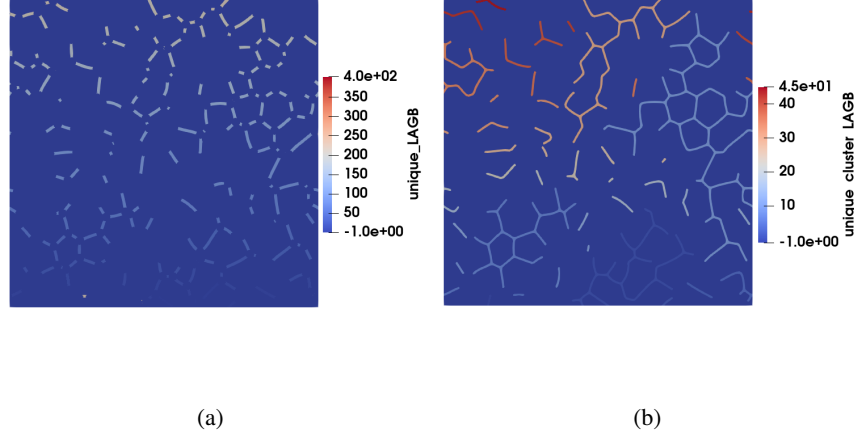


Figure 7.6. One microstructure distinguished by Grain Tracker feature in MOOSE. (a) shows the unique index of LAGBs; (b) shows the unique index of LAGB clusters.

parameters from Section 7.2.4 to see which one better correlates to effective diffusivity. Based on the results presented in Section 7.2.2, we used the GB diffusivities obtained using the potential from Ref. [61].

The effective Ag diffusivity in SiC as a function of temperature, flux, minor axis, and percolation parameter can be described as

$$D^{eff,total}(T, F, m_i, P) = D^{eff,total,HAGB}(T, F, m_i) D^{eff,perco}(T, P) C^{irr,perco}(T, F, m_i, P), \quad (7.5)$$

where $D^{eff,total,HAGB}(T, F, m_i)$ is the diffusivity without impact of percolation fitted from Section 7.2.2, $D^{eff,perco}(T, P)$ is the impact of percolation parameter on effective diffusivity, and $C^{irr,perco}$ accounts for the interaction between percolation and irradiation enhanced diffusivity. Due to the abrupt increase of the effective diffusivity for a high percolation parameter in microstructure, the impact of percolation parameter, $D^{eff,perco}(T, P)$, is fitted to the exponential equation to obtain the pre-factor D_0^{perco} and C^{perco} . These coefficients are described as functions of temperature and are presented in Fig. 7.9. The impact of percolation parameter on effective Ag diffusivity in SiC as a function of temperature and percolation parameter can be described as

$$D^{eff,perco}(T, P) = \left(D_{0,0}^{perco} + D_{0,1}^{perco} T \right) \exp \left(\left(C_0^{perco} + \frac{C_1^{perco}}{T} \right) P \right), \quad (7.6)$$

where P is the percolation parameters. The values of the coefficients $D_{0,i}^{perco}$ and C_i^{perco} depend on the definition used for P as follows:

- When P is the fraction by number of LAGB, f_{num} , the coefficients are $D_{0,0}^{perco} = 0.135$, $D_{0,1}^{perco} = 3.79 \times 10^{-4} K^{-1}$, $C_0^{perco} = -1.26$, and $C_1^{perco} = 7.74 \times 10^3 K$. The quality of the fit for the $D_0^{perco}(T)$, $C^{perco}(T)$,

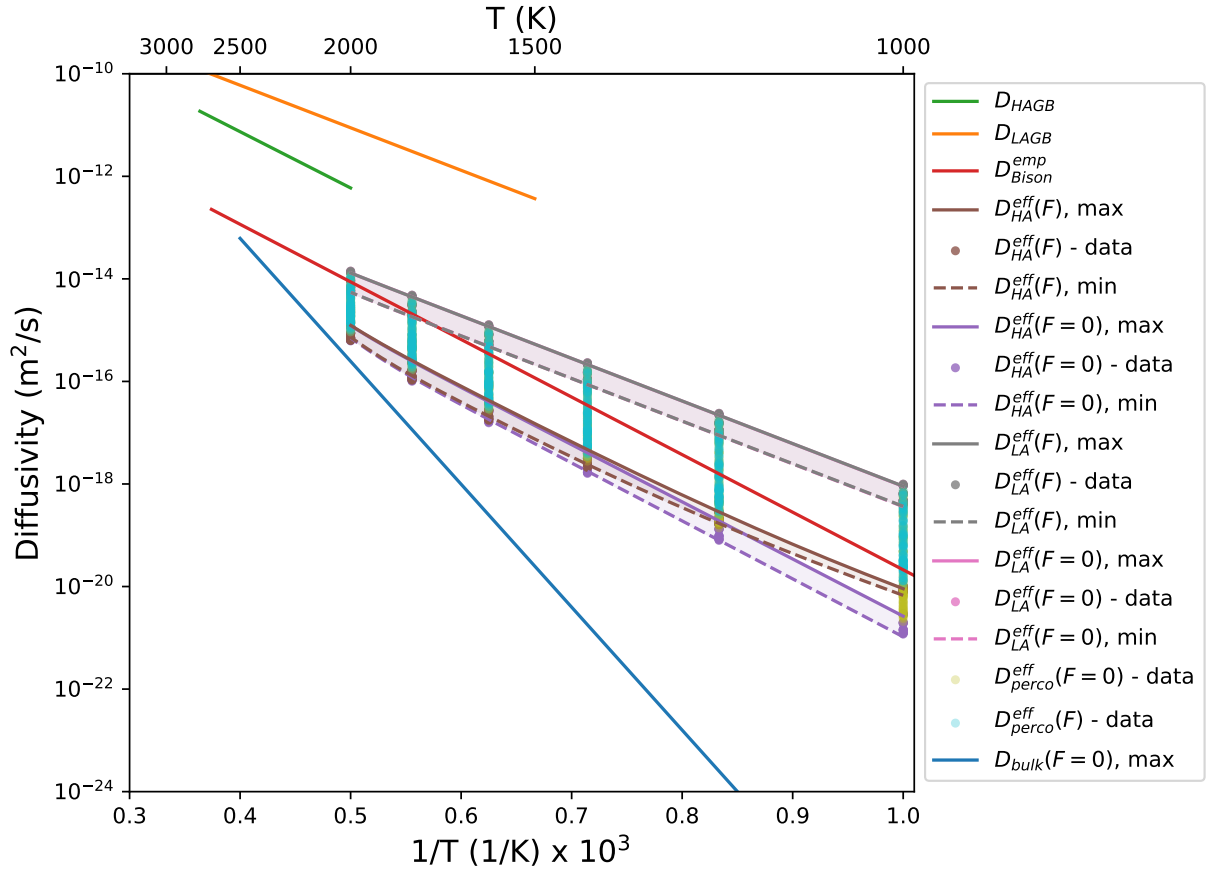


Figure 7.7. Comparison of the Ag diffusion coefficients provided by atomistic simulations with GB diffusivity of higher activation energy (bulk diffusivity, HAGB diffusivity, and LAGB diffusivity) [3], the empirical coefficient D_{BISON}^{emp} previously used in BISON [14, 62, 1, 63], and the effective Ag diffusivity values provided by the current mesoscale study $D^{eff,tot}$ for Ag, including percolation effects (dots). The different values for $D^{eff,tot}$ at each temperature correspond to the extreme grain minor axis length values of the SiC microstructures described in Section 4.1 (solid line for smallest minor axis size, dashed lines for largest minor axis size), and different flux values ($D^{eff,tot}$ for 0 flux, $D^{eff,tot}(F)$ for flux = 4.7×10^{17} n/m²/s).

and $D^{eff,perco}(T, P)$ are equal to $R^2 = 0.997$, $R^2 = 0.994$, and $R^2 = 0.924$, respectively.

- When P is the fraction by area of LAGB, f_{area} , the coefficients are $D_{0,0}^{perco} = 0.108$, $D_{0,1}^{perco} = 3.89 \times 10^{-4} K^{-1}$, $C_0^{perco} = -1.26$, and $C_1^{perco} = 7.73 \times 10^3 K$. The quality of the fit for the $D_0^{perco}(T)$, $C^{perco}(T)$ and $D^{eff,perco}(T, P)$ are equal to $R^2 = 0.996$, $R^2 = 0.994$, and $R^2 = 0.917$, respectively.
- When P is the LAGB cluster strength, $s_{cluster}$, the coefficients are $D_{0,0}^{perco} = 1.65$, $D_{0,1}^{perco} = -1.27 \times 10^{-4} K^{-1}$, $C_0^{perco} = -1.17$, and $C_1^{perco} = 6.46 \times 10^3 K$. The quality of the fit for the $D_0^{perco}(T)$, $C^{perco}(T)$ and $D^{eff,perco}(T, P)$

are equal to $R^2 = 0.975$, $R^2 = 0.995$, and $R^2 = 0.830$, respectively.

- When P is the weighted average length of LAGB cluster, $L_{cluster}$, the coefficients are $D_{0,0}^{perco} = 0.325$, $D_{0,1}^{perco} = 3.68 \times 10^{-4} K^{-1}$, $C_0^{perco} = -1.07$, $C_1^{perco} = 5.91 \times 10^3 K$. The quality of the fit for the $D_0^{perco}(T)$, $C^{perco}(T)$ and $D^{eff,perco}(T, P)$ are equal to $R^2 = 0.969$, $R^2 = 0.996$, and $R^2 = 0.720$, respectively.

The impact of flux on effective Ag diffusivity in SiC as a function of temperature, flux, minor axis, and percolation parameter can be described as

$$C^{irr,perco}(T, F, m_i, P) = 1 + c_0^{irr} \left(\frac{F}{F_0} \right)^{c_1^{irr}} (1 + c_2^{irr} m_i) \exp \left(\frac{c_3^{irr}}{RT} - \frac{c_4^{irr}}{1 - P} \right). \quad (7.7)$$

The calculated effective diffusivity and fitted effective diffusivity are presented in Fig. 7.10. The values of the coefficients c_i^{irr} depend on the definition used for P .

- When P is the fraction by number of LAGB, f_{num} , the coefficients are $c_0^{irr} = 1.09 \times 10^{-11} (n/m^2/s)^{-1}$, $c_1^{irr} = 0.424$, $c_2^{irr} = 3.20 m^{-1}$, $c_3^{irr} = 7.52 \times 10^4 J/mol$, and $c_4^{irr} = 0.578$.
- When P is the fraction by area of LAGB, f_{area} , the coefficients are $c_0^{irr} = 1.05 \times 10^{-11} (n/m^2/s)^{-1}$, $c_1^{irr} = 0.424$, $c_2^{irr} = 3.33 m^{-1}$, $c_3^{irr} = 7.52 \times 10^4 J/mol$, and $c_4^{irr} = 0.562$.
- When P is the LAGB cluster strength, $s_{cluster}$, the coefficients are $c_0^{irr} = 8.99 \times 10^{-12} (n/m^2/s)^{-1}$, $c_1^{irr} = 0.421$, $c_2^{irr} = 3.68 \times 10^3 m^{-1}$, $c_3^{irr} = 7.48 \times 10^4 J/mol$, and $c_4^{irr} = 0.484$.
- When P is the weighted average length of LAGB cluster, $L_{cluster}$, the coefficients are $c_0^{irr} = 5.27 \times 10^{-12} (n/m^2/s)^{-1}$, $c_1^{irr} = 0.422$, $c_2^{irr} = 4.05 m^{-1}$, $c_3^{irr} = 7.53 \times 10^4 J/mol$, and $c_4^{irr} = 0.0776$.

In Figs. 7.9c, 7.9f, 7.9i and 7.9l, the effective diffusivity of microstructures with an LAGB channel (star label) are in general larger than for microstructures without LAGB channel (point label). A channel corresponds to a continuous LAGB pathway across the microstructure connecting the left and right boundaries of the polycrystal. The channel is one GB cluster across the left and right boundary on polycrystal. Figure 7.8 shows an example of microstructures with and without a channel. Microstructures with an LAGB channel diffuse Ag faster than those without. The large variations in effective diffusivity for microstructures with an LAGB channel shows the importance of the channel width. The fraction by number of LAGB, fraction by area of LAGB, and the LAGB cluster strength were identified in Fig. 7.9 as the best definitions for percolation, as they correlate well with effective diffusivity. However, due to the low accuracy of fraction by number in MOOSE and the similarity with the fraction by number and area, we only compared two percolation definitions: the fraction by area of LAGBs f_{area} and the LAGB cluster strength $s_{cluster}$. Due to the better quality of the fit using f_{area} , we recommend it for the definition of the percolation in SiC to derive an effective Ag diffusivity that accounts for temperature, grain size, texture, and irradiation effects.

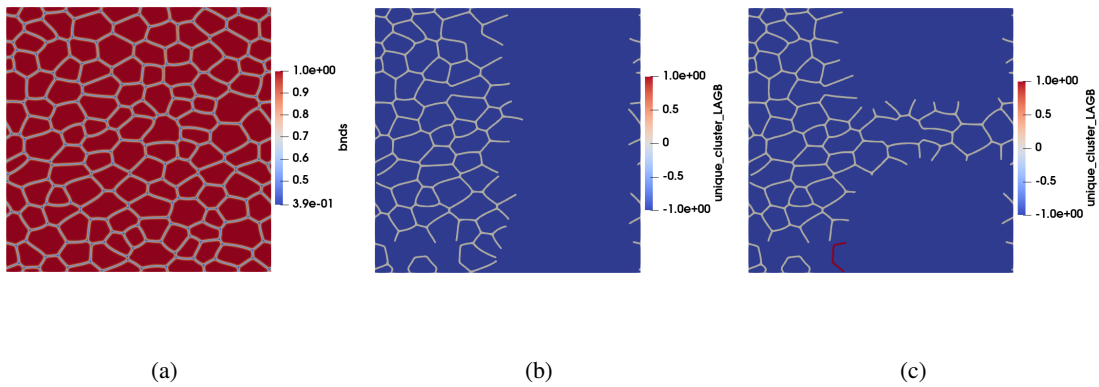


Figure 7.8. Example of a microstructure with different GB type distributions. (a) is the base microstructure; (b, c) show the unique LAGB cluster index with different GB type distributions: (b) has no channel, and (c) has one LAGB channel.

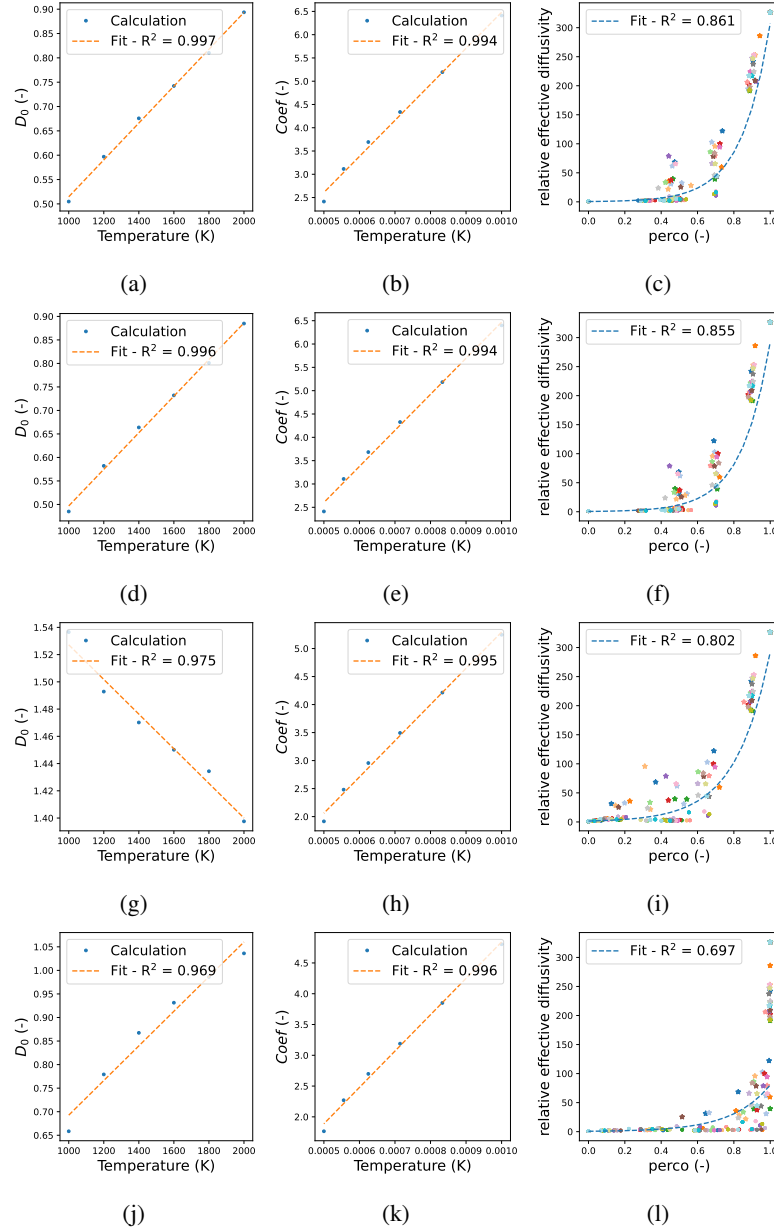


Figure 7.9. Derivation of the percolation contribution to the effective Ag diffusion coefficient as a function of temperature T and different percolation definitions P . (a,b,c) show how (a) D_0^{perco} and (b) C^{perco} depend on T , and (c) shows how $D^{eff,total,perco}$ depends on P at 1000 K when $P = f_{num}$. (d,e,f) show how (d) D_0^{perco} and (e) C^{perco} depend on T , and (f) shows how $D^{eff,total,perco}$ depends on P at 1000 K when $P = f_{area}$. (g,h,i) show how (g) D_0^{perco} and (h) C^{perco} depend on T , and (i) shows how $D^{eff,total,perco}$ depends on P at 1000 K when $P = s_{cluster}$. (j,k,l) show how (j) D_0^{perco} and (k) C^{perco} depend on T , and (l) shows how $D^{eff,total,perco}$ depends on P at 1000 K when $P = L_{cluster}$. In (c,f,i,l), the effective diffusivity of microstructures with an LAGB channel is noted by a star label; others are noted by a point label.

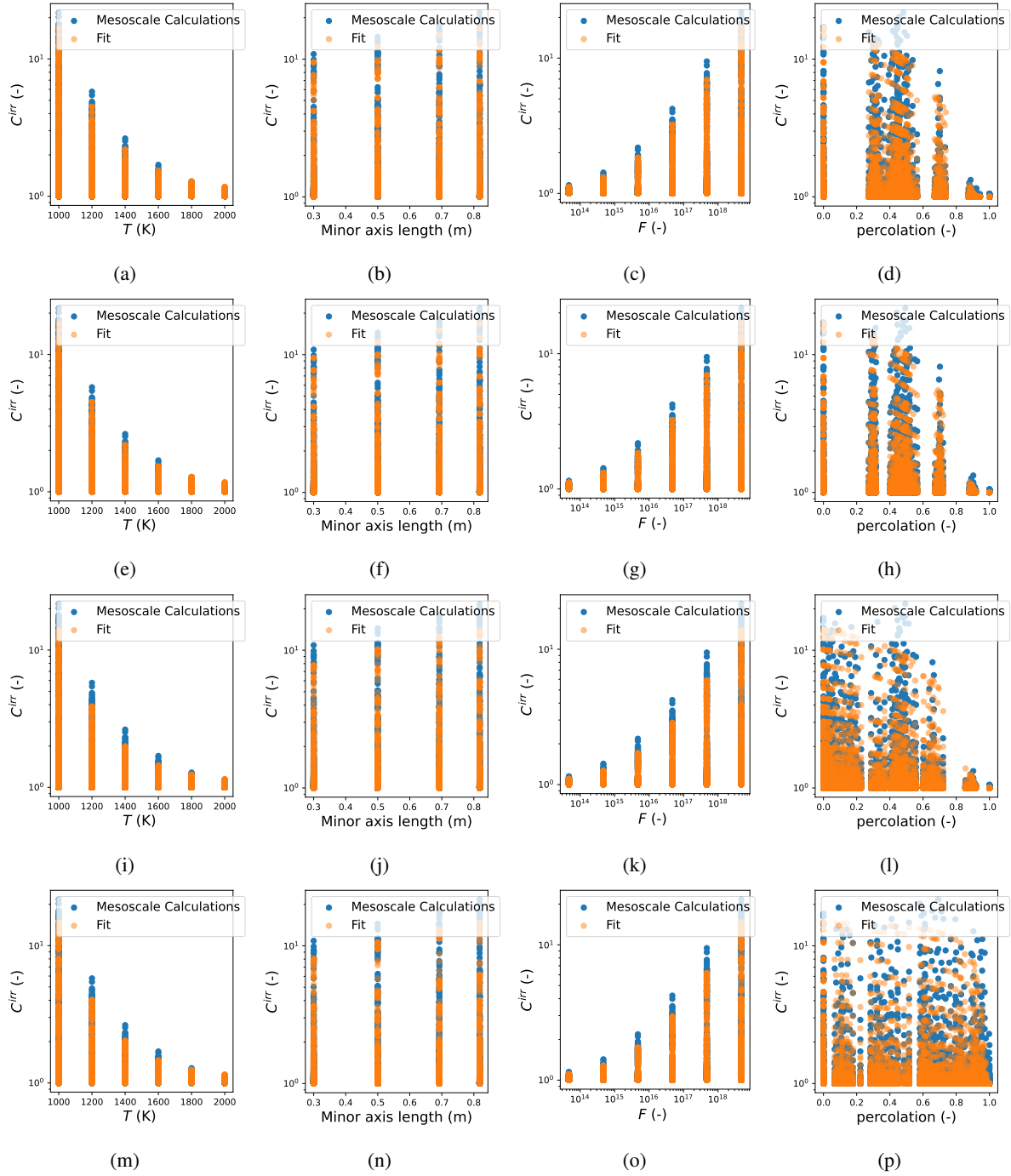


Figure 7.10. Derivation of the flux contribution to the effective Ag diffusion coefficient as a function of temperature T , minor axis m_i , flux F , and different percolation definitions P . (a,b,c,d) show how $C^{irr,perco}$ depends on (a) T , (b) m_i , (c) F , and (d) P when $P = f_{num}$. (e,f,g,h) show how $C^{irr,perco}$ depends on (e) T , (f) m_i , (g) F , and (h) P when $P = f_{area}$. (i,j,k,l) show how $C^{irr,perco}$ depends on (i) T , (j) m_i , (k) F , and (l) P when $P = s_{cluster}$. (m,n,o,p) show how $C^{irr,perco}$ depends on (m) T , (n) m_i , (o) F , and (p) P when $P = L_{cluster}$.

8. OVERALL CONCLUSIONS AND FUTURE WORK

The work presented in this milestone improved our understanding of fission product transport and release from TRISO particles using atomistic, mesoscale, and engineering scale approaches. The three main areas of focus were (1) the development of a multiscale, mechanistic model for Cs diffusion in SiC to understand and predict Cs release from AGR fuel, (2) a preliminary study of Pd attack on SiC at the mesoscale to test initial hypotheses on the mechanism and its potential impact on SiC degradation and accelerated fission product release, and (3) an improvement of the previously published mechanistic model for Ag diffusion in SiC by accounting for texture and different diffusivities at different GB types. Significant progress has been made in all these areas, and the main findings, achievements, conclusions are listed below with suggestions for future work:

- DFT, kMC, and rate theory have been used to determine a temperature and irradiation-dependent bulk diffusivity for Cs in SiC. This effort shows that irradiation-enhanced diffusivity can be significant at low temperatures. Moreover, the approach indicates that the effect of vacancy clustering on radiation-enhanced diffusion in SiC cannot be captured simply by a single binding energy. While the result presented in this report might still be a good approximation for high temperatures where vacancy clusters are not as important as that at low temperatures, a more comprehensive defect model that integrates molecular dynamics and cluster dynamics might be needed to address the complexity involved in the mixed defect cluster formation in SiC.
- This study employed classical MD simulations to investigate the diffusion behavior of Cs and Ag atoms along SiC GBs. To enable these simulations, new empirical potentials for SiC-Cs and SiC-Ag systems have been developed using the ABOP formalism and fitted to DFT-calculated formation energies. The ABOP potential demonstrated reasonable agreement with DFT results for both Cs and Ag. The simulation data revealed that GB diffusion of Cs is significantly slower than Ag, which can be attributed to the larger size of Cs. Interestingly, the MD simulations indicate that diffusion of both Cs and Ag along $\Sigma 5$ GB can be faster than along random HAGBs in SiC, which is contrary to previous assumptions. This finding warrants further investigation through long-time MD simulations using more accurate empirical potentials.
- We used the bulk and GB diffusivities obtained by atomistic calculations to develop an effective Cs diffusivity model in polycrystalline SiC. This new diffusivity model accounts for temperature, microstructure, and irradiation effects. Moreover, it mechanistically explains the experimentally observed two temperature regimes of Cs diffusivity in SiC. The high-temperature regime ($T > 2000$ K) is attributed to the dominance of bulk diffusivity, whereas GB diffusivity dominates at low temperatures. To the authors' knowledge, this is the first modeling

approach that elucidates this phenomena. However, it was found that the model was better validated with a lower GB diffusivity than the value that was determined using MD. The need for further investigation through long-time MD simulations listed above is therefore echoed here, along with investigations of different GB types.

- The validated mesoscale Cs diffusivity model for SiC was implemented in BISON. Using the new model improved Cs release predictions compared to the empirical model for AGR-1 and AGR-2 compacts. Moreover, it accounts for microstructure and irradiation effects.
- A grand-potential based phase-field model was developed to study Pd attack of SiC. Using 2D simulations, it was demonstrated that under high Pd flux, the slow diffusion of C formed during the silicide formation reaction is responsible for the lamellar microstructure observed in experiments. The ratio of the diffusivity of C to Pd has a strong impact on the microstructure formed during the reaction. As the diffusivity of C decreases compared to that of Pd, the microstructure changes from columnar growth toward lamellar growth. This preliminary work provided new insight about Pd penetration in SiC. Future work will focus on improving the quantitative accuracy of the mesoscale model of Pd attack on SiC and using it to derive predictive models in BISON for Pd penetration and accelerated transport of fission products in the attacked SiC layer. Reaching these goals requires (1) improving the parameterization of the phase-field model, including use of the damped-nested-Newton solve method to allow use of more accurate phase free energies, (2) adding the effect of liquid phase formation, especially relevant as Ag reduces the melting temperature of the system, and (3) studying microstructure evolution with larger domain sizes to understand effect of material properties on the length scale of the lamellar microstructure.
- We improved the effective Ag diffusivity model developed in previous years by accounting for the effect of SiC texture on effective diffusivity. Because atomistic simulations performed thus far have shown that LAGBs diffuse faster than HAGBs in SiC, SiC texture impacts Ag release. To quantify texture, we developed a percolation parameter accounting for the path created by LAGBs across the microstructure. This effort is ongoing, and the resulting effective diffusivity model will account for temperature, grain size, texture, and irradiation effects. Future work should also apply the same approach to the newly developed Cs diffusivity model.

Bibliography

- [1] Jason D Hales et al. “Modeling fission product diffusion in TRISO fuel particles with BISON”. In: *Journal of Nuclear Materials* 548 (2021), p. 152840.
- [2] Johan B. Malherbe. “Diffusion of fission products and radiation damage in SiC”. In: *Journal of Physics D: Applied Physics* 46 (47 Oct. 2013), p. 473001. ISSN: 0022-3727. DOI: 10.1088/0022-3727/46/47/473001. URL: <https://iopscience.iop.org/article/10.1088/0022-3727/46/47/473001><https://iopscience.iop.org/article/10.1088/0022-3727/46/47/473001/meta>.
- [3] C. Jiang et al. *Atomistic and mesoscale simulations to determine effective diffusion coefficient of fission products in SiC*. Idaho National Laboratory, 2021.
- [4] Pierre-Clément A. Simon et al. “Mechanistic calculation of the effective silver diffusion coefficient in polycrystalline silicon carbide: Application to silver release in AGR-1 TRISO particles”. In: *Journal of Nuclear Materials* 563 (May 2022), p. 153669. ISSN: 0022-3115. DOI: 10.1016/J.JNUCMAT.2022.153669. URL: <https://linkinghub.elsevier.com/retrieve/pii/S0022311522001635>.
- [5] Pierre-Clement A Simon et al. *Demonstrate Improved Ag Diffusion and Describe the Basis for Pd Penetration Modeling in SiC*. Idaho National Laboratory, Sept. 2022. URL: <https://www.osti.gov/biblio/1922426>.
- [6] D. Schwen et al. “Rapid multiphase-field model development using a modular free energy based approach with automatic differentiation in MOOSE/MARMOT”. In: *Computational Materials Science* 132 (2017), pp. 36–45. DOI: <https://doi.org/10.1016/j.commatsci.2017.02.017>. URL: <https://www.sciencedirect.com/science/article/pii/S0927025617300885>.
- [7] Richard L. Williamson et al. “BISON: A Flexible Code for Advanced Simulation of the Performance of Multiple Nuclear Fuel Forms”. In: *Nuclear Technology* 207 (7 2021), pp. 954–980. ISSN: 19437471. DOI: 10.1080/00295450.2020.1836940. URL: <https://www.tandfonline.com/doi/abs/10.1080/00295450.2020.1836940>.
- [8] Hyunseok Ko, Izabela Szlufarska, and Dane Morgan. “Cs diffusion in SiC high-energy grain boundaries”. In: *Journal of Applied Physics* 122 (10 Sept. 2017), p. 105901. ISSN: 0021-8979. DOI: 10.1063/1.4989389. URL: <https://aip.scitation.org/doi/abs/10.1063/1.4989389>.
- [9] David Shrader, Izabela Szlufarska, and Dane Morgan. “Cs diffusion in cubic silicon carbide”. In: *Journal of Nuclear Materials* 421 (1-3 Feb. 2012), pp. 89–96. ISSN: 0022-3115. DOI: 10.1016/J.JNUCMAT.2011.11.051.

- [10] E. Friedland et al. "Diffusion behavior of cesium in silicon carbide at $T > 1000\text{ }^{\circ}\text{C}$ ". In: *Nuclear Instruments and Methods in Physics Research Section B: Beam Interactions with Materials and Atoms* 286 (Sept. 2012), pp. 102–107. ISSN: 0168-583X. DOI: 10.1016/J.NIMB.2011.11.048.
- [11] Erich Friedland, Thulani Hlatshwayo, and Nic Van der Berg. "Influence of radiation damage on diffusion of fission products in silicon carbide". In: *physica status solidi c* 10 (2 Feb. 2013), pp. 208–215. ISSN: 1610-1642. DOI: 10.1002/PSSC.201200457. URL: <https://onlinelibrary.wiley.com/doi/full/10.1002/pssc.201200457><https://onlinelibrary.wiley.com/doi/abs/10.1002/pssc.201200457><https://onlinelibrary.wiley.com/doi/10.1002/pssc.201200457>.
- [12] S. S. Dwaraknath and G. S. Was. "The diffusion of cesium, strontium, and europium in silicon carbide". In: *Journal of Nuclear Materials* 476 (Aug. 2016), pp. 155–167. ISSN: 0022-3115. DOI: 10.1016/J.JNUCMAT.2016.04.034.
- [13] S. S. Dwaraknath and G. S. Was. "Radiation enhanced diffusion of cesium, strontium, and europium in silicon carbide". In: *Journal of Nuclear Materials* 474 (June 2016), pp. 76–87. ISSN: 0022-3115. DOI: 10.1016/J.JNUCMAT.2016.02.034.
- [14] Rainer Moormann and Karl Verfondern. "Methodik umfassender probabilistischer Sicherheitsanalysen für zukünftige HTR-Anlagenkonzepte Ein Statusbericht (Stand 1986) Band 3 : Spaltproduktfrelsetzung". In: (1987). ISSN: 0343-7639.
- [15] B.F. Myers. *Cesium Diffusion in Silicon Carbide During Post Irradiation Anneals*. Research Center Julich, 1984.
- [16] Kazuo Minato et al. "Release behavior of metallic fission products from HTGR fuel particles at 1600 to 1900°C". In: *Journal of Nuclear Materials* 202 (1-2 June 1993), pp. 47–53. ISSN: 0022-3115. DOI: 10.1016/0022-3115(93)90027-V.
- [17] Winfried Amian and Detlev Stoeber. "Diffusion of Silver and Cesium in Silicon-Carbide Coatings of Fuel Particles for High-Temperature Gas-Cooled Reactors". In: <https://doi.org/10.13182/NT61-475> 61 (3 1982), pp. 475–486. ISSN: 00295450. DOI: 10.13182/NT61-475. URL: <https://www.tandfonline.com/doi/abs/10.13182/NT61-475>.
- [18] A. N. Gudkov et al. "Behavior of solid fission products in coated fuel particles of a high-temperature gas-cooled reactor". In: *Soviet Atomic Energy* 1990 67:2 67 (2 Aug. 1989), pp. 594–599. ISSN: 1573-8205. DOI: 10.1007/BF01125254. URL: <https://link.springer.com/article/10.1007/BF01125254>.
- [19] K. Fukuda et al. *Research and development of HTGR fuel at JAERI*. 1989. URL: http://inis.iaea.org/Search/search.aspx?orig_q=RN:22026511.
- [20] Toru Ogawa et al. *Release of Metal Fission Products from Coated Particle Fuel – Swept-Gas Capsule 74F9J, 75F4A and 75F5A*. Tokai research Establishment, JAERI, Feb. 1985.
- [21] Christ. *Nachrechnung von Ausheizexperimenten*. HRB, 1985.
- [22] K. Verfondern and D. Mueller. *Modelling of fission product release behavior from HTR spherical fuel elements under accident conditions*. 1991. URL: http://inis.iaea.org/Search/search.aspx?orig_q=RN:23008798.

- [23] H.J. Allelein, P. Biedermann, and D. Stoeber. *Cs release from TRISO fuel particles*. 1980. URL: http://inis.iaea.org/Search/search.aspx?orig_q=RN:11519059.
- [24] Jeremy Rabone, Eddie López-Honorato, and Paul Van Uffelen. “Silver and cesium diffusion dynamics at the β -SiC $\Sigma 5$ grain boundary investigated with density functional theory molecular dynamics and metadynamics”. In: *Journal of Physical Chemistry A* 118 (5 Feb. 2014), pp. 915–926. ISSN: 10895639. DOI: 10.1021/JP411156C/SUPPL_FILE/JP411156C_SI_001.PDF. URL: <https://pubs.acs.org/doi/full/10.1021/jp411156c>.
- [25] R Devanathan, WJ Weber, and F Gao. “Atomic scale simulation of defect production in irradiated 3C-SiC”. In: *Journal of Applied Physics* 90.5 (2001), pp. 2303–2309.
- [26] G. Henkelman, B. Uberuaga, and H. Jónsson. “A climbing image nudged elastic band method for finding saddle points and minimum energy paths”. In: *Journal of Chemical Physics* 113 (2000), pp. 9901–9904.
- [27] Jia-Hong Ke et al. “Flux effects in precipitation under irradiation – Simulation of Fe-Cr alloys”. In: *Acta Materialia* 164 (2019), pp. 586–601. ISSN: 1359-6454. DOI: <https://doi.org/10.1016/j.actamat.2018.10.063>. URL: <https://www.sciencedirect.com/science/article/pii/S1359645418308735>.
- [28] Jia-Hong Ke and Benjamin W. Spencer. “Cluster dynamics modeling of Mn-Ni-Si precipitates coupled with radiation-induced segregation in low-Cu reactor pressure vessel steels”. In: *Journal of Nuclear Materials* 569 (2022), p. 153910. ISSN: 0022-3115. DOI: <https://doi.org/10.1016/j.jnucmat.2022.153910>. URL: <https://www.sciencedirect.com/science/article/pii/S0022311522003968>.
- [29] S. Plimpton. “Fast parallel algorithms for short-range molecular dynamics”. In: *J. Comput. Phys.* 117 (1995), pp. 1–19.
- [30] D. W. Brenner. “Empirical potential for hydrocarbons for use in simulating the chemical vapor deposition of diamond films”. In: *Phys. Rev. B* 42 (1990), p. 9458.
- [31] Pierre-Clément Simon et al. “Jupyter script for automatic polycrystalline generation with desired grain size and elongation.” In: 1 (2021). DOI: 10.17632/VH78XYY85F.1.
- [32] Pierre-Clément Simon. “Phase field modeling and quantification of zirconium hydride morphology”. The Pennsylvania State University, Jan. 2021. URL: <https://etda.libraries.psu.edu/catalog/18631pjs5523>.
- [33] Tyler J. Gerczak et al. “SiC layer microstructure in AGR-1 and AGR-2 TRISO fuel particles and the influence of its variation on the effective diffusion of key fission products”. In: *Journal of Nuclear Materials* 480 (Nov. 2016), pp. 257–270. ISSN: 0022-3115. DOI: 10.1016/J.JNUCMAT.2016.08.011.
- [34] Cody J. Permann et al. “Order parameter re-mapping algorithm for 3D phase field model of grain growth using FEM”. In: *Computational Materials Science* 115 (Apr. 2016), pp. 18–25. ISSN: 0927-0256. DOI: 10.1016/J.COMMATSCI.2015.12.042.
- [35] J. D. Hales et al. “Asymptotic expansion homogenization for multiscale nuclear fuel analysis”. In: *Computational Materials Science* 99 (Mar. 2015), pp. 290–297. ISSN: 09270256. DOI: 10.1016/j.commatsci.2014.12.039.
- [36] Michael R. Tonks et al. “An object-oriented finite element framework for multiphysics phase field simulations”. In: *Computational Materials Science* 51 (1 Jan. 2012), pp. 20–29. ISSN: 09270256. DOI: 10.1016/j.commatsci.2011.07.028.

- [37] Cody J. Permann et al. “MOOSE: Enabling massively parallel multiphysics simulation”. In: *SoftwareX* 11 (Jan. 2020), p. 100430. ISSN: 23527110. DOI: 10.1016/j.softx.2020.100430.
- [38] Derek Gaston et al. “MOOSE: A parallel computational framework for coupled systems of nonlinear equations”. In: *Nuclear Engineering and Design* 239 (10 Oct. 2009), pp. 1768–1778. ISSN: 00295493. DOI: 10.1016/j.nucengdes.2009.05.021.
- [39] Blaise P. Collin. “AGR-1 Irradiation Test Final As-Run Report, Rev. 3”. In: (Jan. 2015). DOI: 10.2172/1173081.
- [40] J.D. Hunn et al. *AGR-1 Post Irradiation Examination Final Report, Idaho National Laboratory*. Idaho National Laboratory ID. INL/EXT-15e36407, 2015.
- [41] Eddie López-Honorato et al. “Effect of Microstructure on the Resilience of Silicon Carbide to Palladium Attack”. In: *Journal of the American Ceramic Society* 93.12 (Sept. 2010), pp. 4135–4141. DOI: 10.1111/j.1551-2916.2010.04005.x. URL: <https://doi.org/10.1111/j.1551-2916.2010.04005.x>.
- [42] E.J. Olivier and J.H. Neethling. “The role of Pd in the transport of Ag in SiC”. In: *Journal of Nuclear Materials* 432.1-3 (Jan. 2013), pp. 252–260. DOI: 10.1016/j.jnucmat.2012.07.033. URL: <https://doi.org/10.1016/j.jnucmat.2012.07.033>.
- [43] I. Karakaya and W. T. Thompson. “The Ag-Pd (Silver-Palladium) system”. In: *Bulletin of Alloy Phase Diagrams* 9.3 (June 1988), pp. 237–243. DOI: 10.1007/bf02881271. URL: <https://doi.org/10.1007/bf02881271>.
- [44] Han Liu et al. “A study of reaction between palladium, palladium silver alloy and silicon carbide ceramics at high temperature”. In: *Journal of the European Ceramic Society* 43.8 (July 2023), pp. 3077–3089. DOI: 10.1016/j.jeurceramsoc.2023.02.032. URL: <https://doi.org/10.1016/j.jeurceramsoc.2023.02.032>.
- [45] Han Liu, Philip Withers, and Ping Xiao. “High temperature degradation of silicon carbide (sic) by metallic fission products (Palladium, silver) and oxidation”. PhD thesis. 2017.
- [46] A.A. Kodentsov, M.R. Rijnders, and F.J.J. van Loo. “Periodic pattern formation in solid state reactions related to the Kirkendall effect”. In: *Acta Materialia* 46.18 (Nov. 1998), pp. 6521–6528. DOI: 10.1016/s1359-6454(98)00309-7. URL: [https://doi.org/10.1016/s1359-6454\(98\)00309-7](https://doi.org/10.1016/s1359-6454(98)00309-7).
- [47] Long-Qing Chen. “Phase-Field Models for Microstructure Evolution”. In: *Annual Review of Materials Research* 32.1 (Aug. 2002), pp. 113–140. DOI: 10.1146/annurev.matsci.32.112001.132041. URL: <https://doi.org/10.1146/annurev.matsci.32.112001.132041>.
- [48] Nele Moelans, Bart Blanpain, and Patrick Wollants. “An introduction to phase-field modeling of microstructure evolution”. In: *Calphad* 32.2 (June 2008), pp. 268–294. DOI: 10.1016/j.calphad.2007.11.003. URL: <https://doi.org/10.1016/j.calphad.2007.11.003>.
- [49] Michael R Tonks and Larry K Aagesen. “The phase field method: mesoscale simulation aiding material discovery”. In: *Annual Review of Materials Research* 49 (2019), pp. 79–102.
- [50] Mathis Plapp. “Unified derivation of phase-field models for alloy solidification from a grand-potential functional”. In: *Physical Review E* 84.3 (2011). DOI: 10.1103/physreve.84.031601.

- [51] Larry K. Aagesen et al. “Grand-potential-based phase-field model for multiple phases, grains, and chemical components”. In: *Physical Review E* 98.2 (2018). DOI: 10.1103/physreve.98.023309.
- [52] N. Moelans, B. Blanpain, and P. Wollants. “Quantitative analysis of grain boundary properties in a generalized phase field model for grain growth in anisotropic systems”. In: *Physical Review B* 78.2 (2008). DOI: 10.1103/physrevb.78.024113.
- [53] Nele Moelans. “A quantitative and thermodynamically consistent phase-field interpolation function for multi-phase systems”. In: *Acta Materialia* 59.3 (Feb. 2011), pp. 1077–1086. DOI: 10.1016/j.actamat.2010.10.038. URL: <https://doi.org/10.1016/j.actamat.2010.10.038>.
- [54] Zhenmin Du et al. “A thermodynamic description of the Pd–Si–C system”. In: *Intermetallics* 14.5 (May 2006), pp. 560–569. DOI: 10.1016/j.intermet.2005.09.008. URL: <https://doi.org/10.1016/j.intermet.2005.09.008>.
- [55] Chao Jiang, Isabella J. van Rooyen, and Subhashish Meher. “Ab initio study and thermodynamic modeling of the Pd–Si–C system”. In: *Computational Materials Science* 171 (Jan. 2020), p. 109238. DOI: 10.1016/j.commatsci.2019.109238. URL: <https://doi.org/10.1016/j.commatsci.2019.109238>.
- [56] R. G. Munro. “Material Properties of a Sintered α -SiC”. In: *Journal of Physical and Chemical Reference Data* 26.5 (Sept. 1997), pp. 1195–1203. DOI: 10.1063/1.556000. URL: <https://doi.org/10.1063/1.556000>.
- [57] Matthew Guziewski et al. “Microscopic and Macroscopic Characterization of Grain Boundary Energy and Strength in Silicon Carbide via Machine-Learning Techniques”. In: *ACS Applied Materials Interfaces* 13.2 (Jan. 2021), pp. 3311–3324. DOI: 10.1021/acsami.0c15980. URL: <https://doi.org/10.1021/acsami.0c15980>.
- [58] T.M. Weilert et al. “Effective diffusivity of Ag and migration of Pd in IG-110 graphite”. In: *Journal of Nuclear Materials* 559 (Feb. 2022), p. 153427. DOI: 10.1016/j.jnucmat.2021.153427. URL: <https://doi.org/10.1016/j.jnucmat.2021.153427>.
- [59] Téó Boutin, Werner Verdier, and Alain Cartalade. “Grand-potential-based phase-field model of dissolution/precipitation: Lattice Boltzmann simulations of counter term effect on porous medium”. In: *Computational Materials Science* 207 (May 2022), p. 111261. DOI: 10.1016/j.commatsci.2022.111261. URL: <https://doi.org/10.1016/j.commatsci.2022.111261>.
- [60] Chaitanya Vivek Bhave et al. “An electrochemical mesoscale tool for modeling the corrosion of structural alloys by molten salt”. In: *Journal of Nuclear Materials* 574 (Feb. 2023), p. 154147. DOI: 10.1016/j.jnucmat.2022.154147. URL: <https://doi.org/10.1016/j.jnucmat.2022.154147>.
- [61] Nanjun Chen et al. “Analytical bond-order potential for silver, palladium, ruthenium and iodine bulk diffusion in silicon carbide”. In: *Journal of Physics: Condensed Matter* 32 (2020), p. 085702.
- [62] *Fuel performance and fission product behaviour in gas cooled reactors (Technical Report)* | ETDEWEB. IAEA, Nov. 1997. URL: <https://www.osti.gov/etdeweb/biblio/616984>.

- [63] Blaise P. Collin et al. “Comparison of silver, cesium, and strontium release predictions using PARFUME with results from the AGR-1 irradiation experiment”. In: *Journal of Nuclear Materials* 466 (Nov. 2015), pp. 426–442. ISSN: 0022-3115. DOI: 10.1016/J.JNUCMAT.2015.08.033.
- [64] JA Basinger et al. “Two-dimensional grain boundary percolation in alloy 304 stainless steel”. In: *Scripta materialia* 53.8 (2005), pp. 959–963.
- [65] Ying Chen and Christopher A Schuh. “Diffusion on grain boundary networks: Percolation theory and effective medium approximations”. In: *Acta materialia* 54.18 (2006), pp. 4709–4720.
- [66] Megan Frary and Christopher A Schuh. “Grain boundary networks: Scaling laws, preferred cluster structure, and their implications for grain boundary engineering”. In: *Acta Materialia* 53.16 (2005), pp. 4323–4335.